Johann Wolfgang Goethe-Universität
Frankfurt am Main
Institut für Kernphysik

Dielectron cocktail simulation in pp, p–Pb and Pb–Pb collisions at LHC energies

Master thesis

of

İREM ERDEMİR ÖZDEMİR

Supervisor:
Prof. Dr. Harald Appelshäuser

November 2014

Abstract

The measurement of dielectrons (electron-positron pairs) allows to investigate the properties of strongly interacting matter, in particular the Quark-Gluon Plasma (QGP), which is created in relativistic heavy-ion collisions at the LHC. The evolution of the collision can be probed via dielectrons since electrons do not interact strongly and are created during all stages of the collision. One of the interests in dielectron measurements is motivated by possible modifications of the electromagnetic emission spectrum in the QGP, where pp collisions are used as a medium-free reference.
The dielectron spectrum consists of contributions from various processes. In order to estimate contributions of known dielectron sources, simulations of the so-called dielectron cocktail are performed. In this thesis, dielectron cocktails in minimum bias pp collisions at $\sqrt{s} = 7$ TeV, p–Pb collisions at $\sqrt{s_{\mathrm{NN}}} = 5.02$ TeV and in central (0-10%) and semi-central (20-50%) Pb–Pb collisions at $\sqrt{s_{\mathrm{NN}}} = 2.76$ TeV at the LHC are presented.

Abstract

Die Messungen von Dielektronen (Elektron-Positron Paaren) ermöglichen die Eigenschaften von stark wechselwirkender Materie zu erforschen, insbesondere das Quark-Gluon Plasma (QGP), das in relativistischen Schwerionenkollisionen am LHC erzeugt wird. Die Entwicklung der Kollision kann durch Dielektronen untersucht werden, da Elektronen nicht stark wechselwirken und in allen Phasen der Kollision erzeugt werden. Mögliche Änderungen des elektromagnetischen Emissionsspektrums im QGP sind von Interesse bei Dielektronen-Messungen und pp-Kollisionen werden da als medium-freie Referenz verwendet.
Das Dielektronenspektrum besteht aus Beiträgen von verschiedenen Prozessen. Um Beiträge von bekannten Dielektronenquellen abzuschätzen, werden Simulationen des sogenannten Dielektronencocktails durchgeführt. Im Rahmen dieser Arbeit wird der Dielektronencocktail in minimum bias pp Kollisionen bei $\sqrt{s} = 7$ TeV, p–Pb Kollisionen bei $\sqrt{s_{\mathrm{NN}}} = 5.02$ TeV und in zentralen (0-10%) and semi-zentralen (20-50%) Pb–Pb Kollisionen bei $\sqrt{s_{\mathrm{NN}}} = 2.76$ TeV am LHC vorgestellt.

Contents

1. Introduction

Theoretical calculations predict that hadronic matter at extreme temperatures and densities, for example shortly after the Big Bang or in cold neutron stars, undergoes a phase transition from a hadronic gas to a new state of matter where quarks and gluons are not confined inside the hadrons anymore. This deconfined state of quarks and gluons is called the Quark-Gluon Plasma (QGP) [1, 2]. The theory which predicts the phase transition of matter is the fundamental theory of strong interactions which is called Quantum ChromoDynamics (QCD), and to explore properties of matter under extreme conditions is the object of heavy-ion physics. Experiments dedicated to relativistic heavy-ion collisions, where heavy nuclei such as lead (^{208}Pb) are collided at very high energies, allow to re-create similar conditions in the laboratory for the QGP formation and they take place at the LHC (Large Hadron Collider) and at the SPS (Super Proton Synchrotron) at CERN (Conseil Européen pour la Recherche Nucléaire - the European Organization for Nuclear Research) and at the RHIC (Relativistic Heavy-Ion Collider) at Brookhaven National Laboratory (BNL). Moreover, in the near future at FAIR (Facility for Antiproton and Ion Research) in Darmstadt the QGP phase at high baryon densities will be studied.

In a relativistic heavy-ion collision there are several stages as illustrated in Figure 1.1.

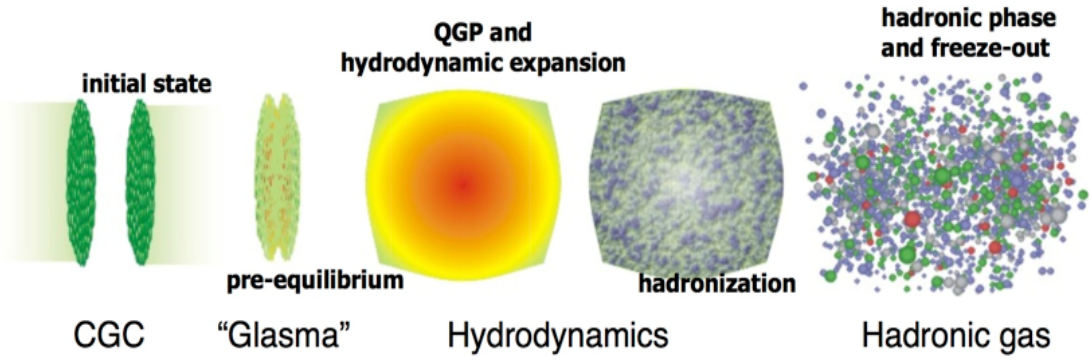

Figure 1.1.: Stages of a relativistic heavy-ion collision [3].

The QGP formation, the central stage of the collision, occurs with the expansion of the fireball created in the initial impact between two nuclei. Then the evolution of the fireball continues with cooling down to the final freeze-out. There are two types of freeze-out. One of them is the *chemical freeze-out* where inelastic collisions between the particles cease. The fireball achieves at the chemical freeze-out stage its final particle composition. The other one is the *thermal freeze-out* where elastic collisions between the particles stop due to the fact that the mean free path of the particles is greater than the size of the fireball.

Figure 1.2 shows the phase diagram of QCD matter as a function of temperature T and net baryon density μ_B. The QGP phase can be reached by heating up the system (e.g. at the LHC/RHIC) and/or by increasing the density (e.g. at FAIR). According to QCD calculations, the first order phase transition into the deconfined phase is expected at some μ_B above a critical point whose exact location is not known precisely. Below the critical point, the transition is a continuous cross over which is expected to be at $T_c \sim 170$ MeV. Another prediction of QCD is the transition into a chirally symmetric phase at a temperature similar to that of the deconfinement transition, so, the QGP can be defined as the deconfined and chirally restored strongly interacting matter [4, 5].

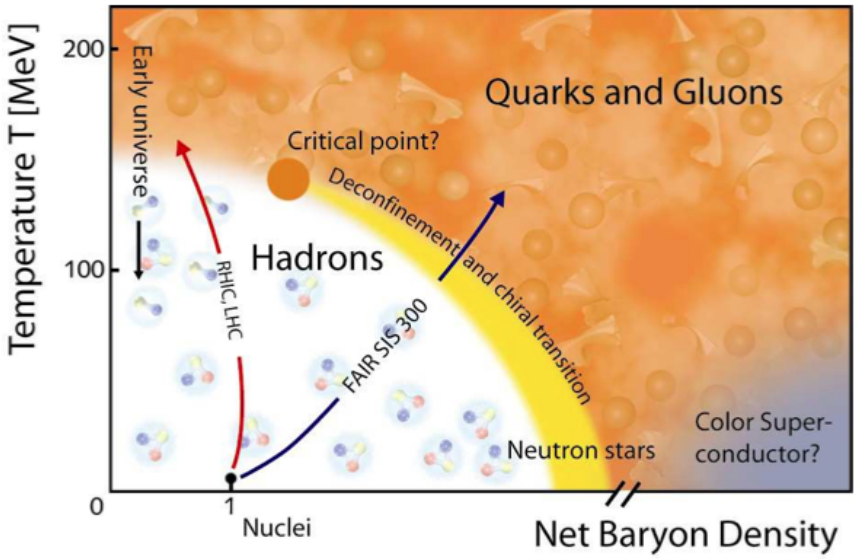

Figure 1.2.: The phase diagram of QCD [6].

The study of properties of hot and dense matter is possible using electromagnetic probes such as dielectrons (electron-positron pairs). Dielectrons are emitted throughout the collision and do not interact strongly, so they have a long mean free path in the medium and leave the medium with negligible final state interaction. Consequently, dielectrons carry information from all phases of the collision and this makes them an important tool to study the QGP. Dielectron sources at different invariant masses are produced at different stages of the collision. Thus, the invariant mass spectrum of dielectrons allows for a chronological view on the evolution of the system. Dielectron sources in the low mass region (e.g. ρ, ω and ϕ) reveal hints on in-medium modifications related to chiral symmetry restoration. In the intermediate mass region, dielectron sources (semileptonic heavy-flavor decays of charm and beauty mesons) are sensitive to thermal radiation of the QGP and prime probes of possible in-medium modifications. Dielectron sources in the high mass region (J/ψ, ψ', Drell-Yan, Υ) allow to study deconfinement effects in hot and dense medium. A dielectron spectrum which consists of expected contributions from known dielectron sources is called dielectron cocktail. It is a simulation in order to interpret the data and so it is used as reference for dielectron measurements.

This thesis is dedicated to dielectron cocktails for proton–proton (pp), proton–lead (p–Pb) and lead–lead (Pb–Pb) collisions in the acceptance of the ALICE (A Large Ion Collider Experiment) detector at the LHC. Dielectrons in pp collisions serve as medium-free baseline for those in Pb–Pb, and those in p–Pb collisions provide the opportunity to study the impact of the cold nuclear matter.

2. Probing hot and dense matter with dielectrons

2.1. The standard model of particle physics

It is supposed that the universe emerged from a Big Bang (∼13.7 billion years ago), which is a theory to explain the expansion of the universe starting from an infinitesimally small volume in which extreme high energy and temperature are concentrated (Figure 2.1). During the expansion, as the universe got cooler, some of energy was converted into pairs of particles and antiparticles with mass ($E = mc^2$). Until 10^{-43} seconds after the Big Bang, the four forces were unified. Firstly, the gravitational force separated from the strong-electro-weak force, at 10^{-43} seconds. Then, at 10^{-35} seconds, the strong force separated from the electro-weak force and thereby quarks, leptons and gauge bosons existed. At 10^{-12} seconds, four fundamental forces became distinctly and leptons began to clump together into electrons, neutrinos and antiparticles. At that point, the universe was filled with a hot Quark-Gluon Plasma (QGP) including leptons and antiparticles. From this point on there were no free quarks, and quarks and antiquarks formed protons and neutrons at 10^{-6} seconds. In the next three minutes after the Big Bang, the protons and neutrons fused to form atomic nuclei. And the evolution continued with the formation of other structures [7].

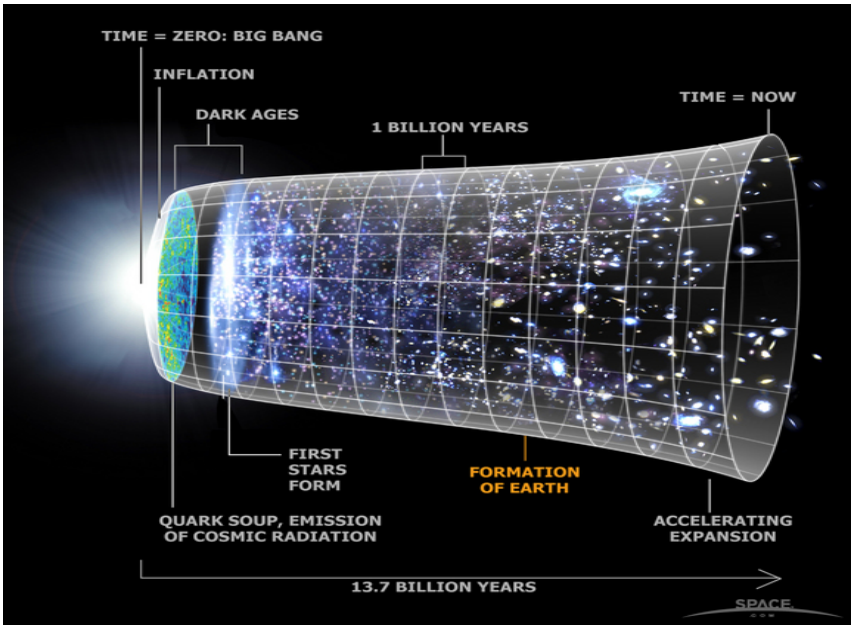

Figure 2.1.: Sketch for history of the universe [7].

Particle physicists predict that the behaviors of all known subatomic particles mentioned above can be described within a single theoretical framework which is called the standard model (SM). In the SM, the fundamental constituents are quarks and leptons and they are known as fermions, i.e. spin-1/2-particles. Fermions are classified in three generations depending on their masses (Table 2.1). Each fermion has an associated antifermion, which is not included in the table, with the same mass but with the opposite electric and color charge. As indicated in Table 2.1, fermions are classified into leptons and quarks. Fermions with non-zero electric/color charge interact electromagnetically/strongly and all fermions interact weakly.

Fermions	Generation			Electric charge	Colour charge
Leptons	ν_e	ν_μ	ν_τ	0	-
	e	μ	τ	-1	
Quarks	u	c	t	+2/3	red, green, blue
	d	s	b	-1/3	

Table 2.1.: The fermions of the standard model.

The SM incorporates three of the four fundamental forces, except gravitation. Each of three fundamental forces of the SM allows the fundamental constituents to interact with each other and is mediated by the exchange of vector bosons (gauge bosons), which are spin-1-particles. With other words, the gauge bosons are force carriers of the fundamental interactions (Table 2.2). The range of the electromagnetic interaction is infinite since photons are massless. In contrast, the range of the strong interaction is confined to about 1 fm even though gluons are also massless. The reason is that gluons have an additional degree of freedom and hence interact with each other. The weak interaction has a limited range, 10^{-3}fm, due to the large mass of its exchange bosons. [8]

Interaction	couples to	Exchange boson(s)	Mass (GeV/c^2)
strong	colour charge	8 gluons (g)	0
electromagnetic	electric charge	photon (γ)	0
weak	weak charge	$W^\pm$, Z^0	∼80, ∼91

Table 2.2.: The interactions and their gauge bosons in the standard model.

2.2. Relativistic heavy-ion collisions

Relativistic heavy-ion collisions allow to probe the QCD matter under extreme conditions. Figure 2.2 depicts the space-time (z,t) evolution of a hot medium created in the overlapping area at t=0 and z=0 of the two passing nuclei. The z-axis is assumed to be the beam direction or the longitudinal direction opposed to the transverse plane, which is vertical to the collision axis. Since these two nuclei collide relativistically, they are squeezed in the direction of the beam axis due to Lorentz contraction. Shortly after the collision of these two nuclei, the QGP is formed in the central rapidity region when the energy density is sufficient. Going through various processes, the created fireball expands in space-time until the created particles freeze out.

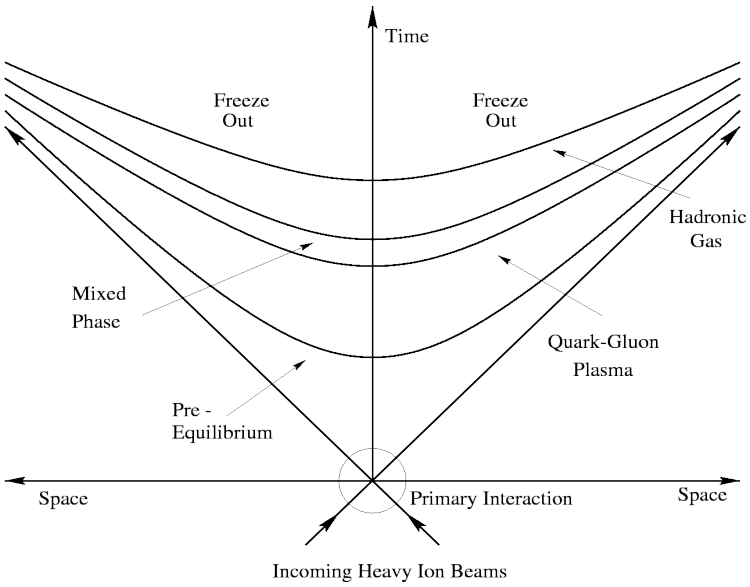

Figure 2.2.: Space-time evolution of a heavy-ion collision [9].

In the following, some variables are introduced for kinematical characterization of particles in a relativistic heavy-ion collision. With the four-momentum vector for relativistic particles $p_\mu = (E, p_\mathrm{x}, p_\mathrm{y}, p_\mathrm{z})$, the transverse momentum is described as follows:

$$p_\mathrm{T} = \sqrt{p_\mathrm{x}^2 + p_\mathrm{y}^2} \tag{2.1}$$

where E is the energy, p_x, p_y and p_z are the components of the three-momentum, and the rapidity can be defined as:

$$y = \frac{1}{2}\ln\left(\frac{E + p_\mathrm{z}}{E - p_\mathrm{z}}\right) \tag{2.2}$$

Here, the rapidity is a quantity which is the relativistic analogue of non-relativistic velocity. In case of a particle emitted at an angle θ relative to the beam axis, the pseudorapidity variable can be used :

$$\eta = \frac{1}{2}\ln\left(\frac{p + p_\mathrm{z}}{p - p_\mathrm{z}}\right) \tag{2.3}$$

where $p = |\mathbf{p}| = \sqrt{p_\mathrm{x}^2 + p_\mathrm{y}^2 + p_\mathrm{z}^2}$ is the three-momentum. For very high energies ($p \gg m$) the mass of the particle is negligible, and thus $y = \eta$. [1, 2]

2.3. Quantum chromodynamics

Since quarks carry color charges (*red, green, blue*) they undergo the strong interaction. In the SM of particle physics, the strong interaction is described by a quantum field theory (QFT) called Quantum ChromoDynamics (QCD). Color charges are the analogue of electric charge in Quantum ElectroDynamics (QED) with an important difference; color charge of quarks is a vector charge and the total color charge "white" of a system is obtained by combining the individual charges according to group theoretical rules. As outlined in Section 2.1, gluons are the force carriers of the strong interaction in analogy to photons in the electromagnetic interaction. However, the key difference between QCD and QED is the self-interaction of gluons, because gluons themselves carry color charges. And these facts are responsible for many of the main characteristics of QCD such as asymptotic freedom, color confinement and chiral symmetry breaking [5, 10].

In the QFT, the interaction strength between two particles is described by the coupling constant depending on the distance r or the four momentum transfer Q^2 between two particles, where $Q^2 \propto 1/r^2$, and the electromagnetic force between two electrons is defined by

$$F = \frac{e^2}{4\pi c\hbar\epsilon_0 r^2} = \frac{\alpha_{em}(r)}{r^2} \tag{2.4}$$

where e is the electric charge, c is the speed of light in vacuum, $\hbar$ is the reduced Planck constant and ϵ_0 is the permittivity of free space. Here, the coupling constant α_{em} depends on Q^2 very weakly, as $r \to \infty$ and $Q^2 \to 0$, and assuming $c = \hbar = \epsilon_0 = 1$:

$$\alpha_{em}(Q^2 \to 0) = \frac{e^2}{4\pi} \approx \frac{1}{137} \tag{2.5}$$

α_{em} is much less than one and this means that higher order interactions play a negligible role in QED. Therefore, it turns out that QED is a strongly-coupled theory only at very short distances. However, in strong interactions the dependence on Q^2 is quite strong:

$$\alpha_s(Q^2) = \frac{g^2}{4\pi} = \frac{12\pi}{(33 - 2n_f)\ln(Q^2/\Lambda^2)} \qquad for\ (Q^2 \gg \Lambda^2), \tag{2.6}$$

where g is the color charge, n_f is the number of quark types and Λ ($\sim$250 MeV/c) is the QCD scale parameter. For very small distances or large momentum transfers the coupling decreases, $\alpha_s \ll 1$. In this regime, quarks behave quasi-freely and this phenomenon is called *asymptotic freedom*. In contrast, for small momentum transfers or large distances, the coupling increases, $\alpha_s \approx 1$, and higher order interactions play an important role. In this case, quarks are confined in hadrons, a phenomenon called *color confinement* (or simply *confinement*). The reason of the dependence of the coupling constant on Q^2 is that gluons carry color charges, so they can couple to other gluons as well. In other words, $\alpha_s(Q^2)$ is not a constant anymore which is also denoted as *running coupling* (Figure 2.3) [8, 10].

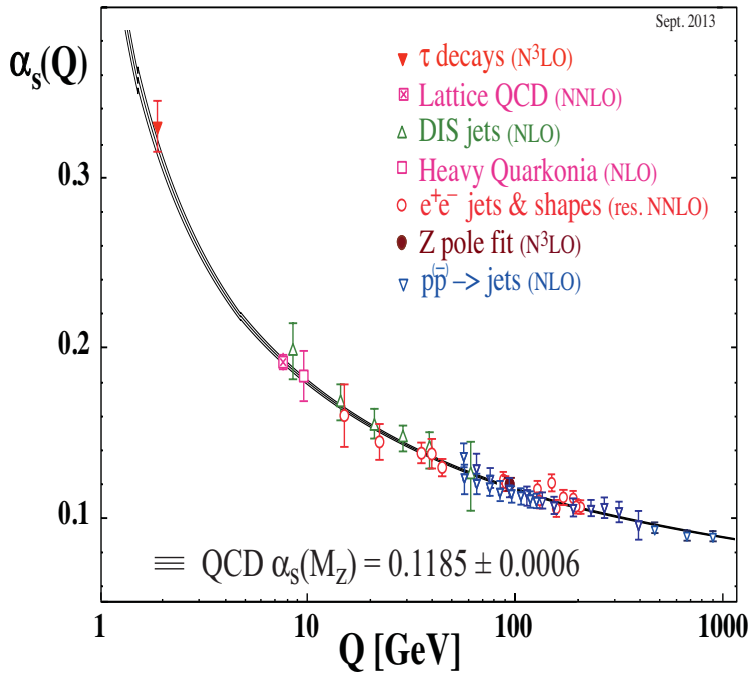

Figure 2.3.: The running coupling constant, α_s, depending on the momentum transfer Q from different experimental results and theoretical prediction [11].

To describe the equation of motion in the SM of particle physics, the Lagrangian density is used. Since quarks are fermions, they obey the Dirac equation and thus the Dirac Lagrangian of quarks follows [12]:

$$\mathcal{L}_q = \bar{\psi}(i\gamma^\mu \partial_\mu - \mathbf{M})\psi \tag{2.7}$$

where $\bar{\psi}$ and ψ are the quark fields, γ^μ are the Dirac matrices and $\mathbf{M}$ = diag(m_u, m_d, m_c, m_s, m_t, m_b) is the diagonal matrix of the approximately bare quark masses with 2 MeV/c^2, 5 MeV/c^2, 95 MeV/c^2, 1.3 GeV/c^2, 4.2 GeV/c^2, 173 GeV/c^2, respectively.
In Equation 2.7, quarks are assumed to be free and the interaction of quarks with 8 gluon fields is not considered. Considering the quark-gluon interaction, Equation 2.7 is extended to:

$$\mathcal{L}_q = \bar{\psi}(i\gamma^\mu D_\mu - \mathbf{M})\psi \qquad with \quad D_\mu = \partial_\mu - ig(\lambda_a/2)A^a_\mu \tag{2.8}$$

where g is the strong coupling, A^a_μ is the spin-1 gluon field with 8 color charges a = (1,...,8) according to the SU(3)-flavor group and λ_a are the Gell-Mann matrices.
The Dirac Lagrangian of quarks was the first term of the QCD Lagrangian. The second term is inserted to the equation for the kinetic part, in order to identify the interaction between the gluons:

$$\mathcal{L}_g = -\frac{1}{4} G^a_{\mu\nu} G^{\mu\nu}_a \tag{2.9}$$

Here, $G^a_{\mu\nu}$ is the field strength tensor for the spin-1 gluon field A^a_μ and defined by:

$$G^a_{\mu\nu} = \partial_\mu A^a_\nu - \partial_\nu A^a_\mu + ig f^{abc} A^b_\mu A^c_\nu \tag{2.10}$$

where f^{abc} is the structure constants of the SU(3)-flavor group.
Including the self-interaction of 8 gluon fields, the QCD Lagrangian becomes:

$$\mathcal{L}_{QCD} = \mathcal{L}_q + \mathcal{L}_g = \bar{\psi}(i\gamma^\mu D_\mu - \mathbf{M})\psi - \frac{1}{4} G^a_{\mu\nu} G^{\mu\nu}_a \tag{2.11}$$

2.3.1. Chiral symmetry

Another main characteristic of QCD is chiral symmetry [5, 13]. Chirality is used to define handedness of a particle and describes the correlation between direction of motion and spin of a particle.
Chiral symmetry provides the understanding of many phenomena in low mass hadron physics involving the light quarks (u, d, s). It is a perfect symmetry in the limit of vanishing quark masses. In this limit, the theory is invariant under global vector and axial-vector transformations in SU(3)-flavor space

$$\psi \to e^{-i\theta_V}\psi \ , \quad \psi \to e^{-i\theta_A\gamma_5}\psi \tag{2.12}$$

with conserved vector and axial-vector Noether currents

$$j_V = \bar{\psi}\gamma^\mu\psi \ , \quad j_A = \bar{\psi}\gamma^\mu\gamma_5\psi \tag{2.13}$$

which means that the corresponding charges commute with the QCD Hamiltonian, namely $[Q_{V,A}, H_{QCD}] = 0$.

If one introduces the following left- and right-handed projections of the quark fields

$$\psi_{\mathrm{L}} = \frac{1}{2}(1-\gamma_5)\psi \ , \quad \psi_{\mathrm{R}} = \frac{1}{2}(1+\gamma_5)\psi \tag{2.14}$$

the QCD Lagrangian takes the form

$$\mathcal{L}_{QCD} = \bar{\psi}_{\mathrm{L}} i\gamma^\mu D_\mu \psi_{\mathrm{L}} + \bar{\psi}_{\mathrm{R}} i\gamma^\mu D_\mu \psi_{\mathrm{R}} - \frac{1}{4} G^a_{\mu\nu} G^{\mu\nu}_a - (\bar{\psi}_{\mathrm{L}}\mathbf{M}\psi_{\mathrm{R}} + \bar{\psi}_{\mathrm{R}}\mathbf{M}\psi_{\mathrm{L}}) \tag{2.15}$$

For $m_q = 0$, the QCD Lagrangian constitutes a global $\mathrm{SU}(3)_{\mathrm{L}} \times \mathrm{SU}(3)_{\mathrm{R}}$ *chiral symmetry* in flavor space. Apart from this symmetry, the QCD Lagrangian has another symmetry which is under global $\mathrm{U}_V(1) \times \mathrm{U}_A(1)$ transformations. However, in the full quantum theory j_A has an anomaly (the $\mathrm{U}_A(1)$ *axial anomaly*) and the axial charge of the vacuum is not zero ($\mathrm{Q}_A|0\rangle \neq 0$). Consequently QCD is symmetric only under the group

$$SU(3)_{\mathrm{L}} \times SU(3)_{\mathrm{R}} \times U_V(1)$$

In this way if the quarks have a finite mass, a mass term in the Lagrangian is always a mixture of chiral partners and a small violation of the chiral symmetry is given by the mass term

$$\mathcal{L}_m = \bar{\psi_{\mathrm{L}}}\mathbf{M}\psi_{\mathrm{R}} + \bar{\psi_{\mathrm{R}}}\mathbf{M}\psi_{\mathrm{L}}$$

of the QCD Lagrangian (Equation 2.15). Therefore, the QCD vacuum does not possess the symmetry of the vacuum, i.e. chiral symmetry is *spontaneously* broken.
The averaged light quark mass results $m_q = (m_u + m_d)/2 \leq 10$ MeV/c^2, which is the scale of *explicit* chiral symmetry breaking. This averaged quark mass compared to typical hadron masses of order 1 GeV/c^2 indicates that the symmetry is excellent and in the exact chiral limit ($m_q = 0$) left- and right-handed quarks decouple.
The appearance of eight nearly massless Goldstone bosons (e.g. pions, kaons, eta with extremely small mass compared to other hadrons), the building-up of a chiral quark condensate $\langle\bar{\psi^q}\,\psi^q\rangle = \langle(\bar{\psi^u}\,\psi^u + \bar{\psi^d}\,\psi^d)/2\rangle$ which explicitly mixes left- and right-handed quarks in the broken vacuum $\langle\bar{\psi^q}\,\psi^q\rangle = \langle(\bar{\psi^q_{\mathrm{L}}}\,\psi^q_{\mathrm{R}} + \bar{\psi^q_{\mathrm{R}}}\,\psi^q_{\mathrm{L}})/2\rangle$, the absence of parity doublets are the evidences originated from spontaneously broken chiral symmetry of the QCD vacuum. However, a partial *restoration* of the chiral symmetry is expected with increasing temperature and density, i.e. with increasing momentum transfer Q^2, where initially confined quarks and gluons become deconfined in heated and compressed matter. That means that chiral symmetry restoration associated with the vanishing of the chiral condensate ($\langle\bar{\psi^q}\,\psi^q\rangle$) occurs at a similar temperature (at $\mathrm{T}_c = 170$ MeV) where the QCD matter undergoes the phase transition from a confined to a deconfined phase [1, 5, 13].

2.4. Mesons in the Quark Model

It is quite important to mention mesons as the main objects of the dielectron cocktail study and to know more about their properties.
In the quark model, mesons are quark-antiquark ($q\bar{q}$) bound states. The existing six flavors of quarks are up(u), down(d), strange(s), charm(c), bottom(b) -which is also known as beauty- and top(t) quarks, and in Table 2.3 a list of them is given with their masses and quantum numbers.

Flavor	Mass	B	j	I	I_z	S	C	B^*	T	Q/e
u	~ 2 MeV/c^2	+1/3	1/2	1/2	+1/2	0	0	0	0	+2/3
d	~ 5 MeV/c^2	+1/3	1/2	1/2	–1/2	0	0	0	0	–1/3
s	~ 95 MeV/c^2	+1/3	1/2	0	0	–1	0	0	0	–1/3
c	~ 1.3 GeV/c^2	+1/3	1/2	0	0	0	1	0	0	+2/3
b	~ 4.2 GeV/c^2	+1/3	1/2	0	0	0	0	–1	0	–1/3
t	~ 173 GeV/c^2	+1/3	1/2	0	0	0	0	0	1	+2/3

Table 2.3.: Quarks with their quantum numbers denoted with B: baryon number, j: spin, I: isospin, I_z: isospin z-component, S: strangeness, C: charm, B^*: bottomness, T: topness, Q/e: electric charge.

Assuming that quark-antiquark combinations of the lowest-lying mesons do not have any relative orbital angular momentum (ℓ=0) and recalling that quarks and antiquarks have opposite intrinsic parities, P [1] = -1, the quark spins will determine the mesonic total angular momentum J [2]. Consequently, the $J^P = 0^-$ states are referred to as *pseudoscalar mesons* while the $J^P = 1^-$ states are *vector mesons*.

Heavy quark-antiquark pairs with the same flavor such as $c\bar{c}$, $b\bar{b}$ and $t\bar{t}$ are known as *quarkonia*. Due to very short lifetime of the top quark, the hypothetical *toponium* $t\bar{t}$ does not exist. Therefore, quarkonia refer only to the *charmonium* $c\bar{c}$ and *bottonium* $b\bar{b}$. The lowest-lying state of $c\bar{c}$ is $\eta_c(1S)$ [14] with $J^P = 0^-$. $J/\psi(1S)$ [15, 16] with $J^P = 1^-$ is the first excited state of $c\bar{c}$ and $\psi(2S)$ known as ψ' with $J^P = 1^-$ is the first excited state of J/ψ. As in the case of the charmonium, there is bound states of heavier beauty quarks. The lowest-lying state of $b\bar{b}$ is $\eta_b(1S)$ [17] with $J^P = 0^-$ and its first excited state is $\Upsilon(1S)$ [18, 19] with $J^P = 1^-$.
Since the charmonium and bottonium have very different masses, they can be easily distinguished from each other. But in case of the light quarks (u, d and s), the masses of the quarks are so similar to each other that one can not distinguish the mesons according to their quark content.
Considering only the light quarks u, d, s and antiquarks $\bar{u}$, $\bar{d}$,$\bar{s}$, one can form $3 \otimes \bar{3} = 9$ isospin combinations. In Table 2.4, the nine pseudoscalar meson states are summarized. In this 0^- nonet, the π^0 meson forms an isospin triplet together with the π^+ and π^-. Additionally, the actual states of η and η' appear to be linear combinations of the wave functions of η_8 and η_0.

I	I_z	S	Wavefunction	Q/e
1	1	0	$u\bar{d} = \pi^+$	+1
1	–1	0	$\bar{u}d = \pi^-$	–1
1	0	0	$\frac{1}{\sqrt{2}}(d\bar{d} - u\bar{u}) = \pi^0$	0
1/2	1/2	+1	$u\bar{s} = K^+$	+1
1/2	–1/2	+1	$d\bar{s} = K^0$	0
1/2	–1/2	–1	$\bar{u}s = K^-$	–1
1/2	1/2	–1	$\bar{d}s = \bar{K^0}$	0
0	0	0	$\frac{1}{\sqrt{6}}(d\bar{d} + u\bar{u} - 2s\bar{s}) = \eta_8$	0
0	0	0	$\frac{1}{\sqrt{3}}(d\bar{d} + u\bar{u} + s\bar{s}) = \eta_0$	0

Table 2.4.: Pseudoscalar meson states as quark-antiquark combinations.

Table 2.5 shows the nine vector meson states. One can note that nearly equal masses are predicted for the ρ and ω mesons, and they are interpreted as mixed states of the u and d quarks. Similarly to pions in the pseudoscalar meson states, the ρ^0 meson forms an isospin triplet together with the ρ^+ and ρ^- [8, 20].

[1] The parity P is a symmetry in terms of space reflection and it is $(-1)^{(\ell+1)}$ = -1 for mesons with $\ell = 0$.
[2] The total angular momentum J corresponds to $\ell+j$, where ℓ stands for the orbital angular momentum. Assuming that mesons are in a state of ℓ=0, the total angular momentum corresponds to the total spin ($j = 1$ or $j = 0$). In that case, one might expect both spin-triplet ($\uparrow\uparrow$) states with J = 1 and spin-singlet ($\downarrow\uparrow$) states with J = 0.

I	I_z	S	Wavefunction	Q/e
1	1	0	$u\bar{d} = \rho^+$	+1
1	–1	0	$\bar{u}d = \rho^-$	–1
1	0	0	$\frac{1}{\sqrt{2}}(u\bar{u} - d\bar{d}) = \rho^0$	0
1/2	1/2	+1	$u\bar{s} = K^{*+}$	+1
1/2	–1/2	–1	$s\bar{u} = K^{*-}$	–1
1/2	–1/2	+1	$d\bar{s} = K^{*0}$	0
1/2	1/2	–1	$s\bar{d} = \bar{K^{*0}}$	0
0	0	0	$\frac{1}{\sqrt{2}}(u\bar{u} + d\bar{d}) = \omega$	0
0	0	0	$s\bar{s} = \phi$	0

Table 2.5.: Vector meson states as quark-antiquark combinations.

2.5. Dielectron spectrum

Dielectrons are ideal tools to probe strongly interacting matter. On the one hand, they are emitted at all stages of a heavy-ion collision. On the other hand, they leave the medium created in the collision with negligible final state interaction due to the fact that they do not undergo strong interactions. Through these attributes, dielectrons carry signals unaffectedly from their production vertex into the detector and provide hints about the initial state of the collision. However, the measurement of dielectrons is challenging due to their small production cross sections.

Main properties of known dielectron sources treated in this dielectron cocktail study are listed in Table 2.6 and Table 2.7.

Particle	Mass (MeV/c^2)	Decay channel	Branching ratio	Decay width (MeV/c^2)
π^0	134.9766	$e^+e^-\gamma$	1.174×10^{-2}	8.2×10^{-6}
η	547.853	$e^+e^-\gamma$	6.9×10^{-3}	1.30×10^{-3}
ρ	775.49	e^+e^-	4.72×10^{-5}	146.2
ω	782.65	$e^+e^-\pi^0$, e^+e^-	7.7×10^{-4},7.28×10^{-5}	8.49
η'	957.78	$e^+e^-\gamma$	$< 9\times10^{-4}$	0.239
ϕ	1019.455	$e^+e^-\eta$, e^+e^-	1.15×10^{-4},2.954×10^{-4}	4.26
J/ψ	3096.916	$e^+e^-\gamma$, e^+e^-	8.8×10^{-3} ,5.94×10^{-2}	92.9×10^{-3}

Table 2.6.: Hadronic dielectron sources.

Continuum	Decay channel	Branching ratio
$c\bar{c}$	e^+e^- from $c \to$e and $\bar{c} \to$e	0.103
$b\bar{b}$	e^+e^- from $b(\to c)\to$e and $\bar{b}(\to \bar{c}) \to$e	0.205

Table 2.7.: Semileptonic dielectron sources.

The invariant mass of an electron-positron pair enables us to access to its parent and it is defined as

$$m_{e^+e^-} \cdot c^2 = \sqrt{(E_{e^+} + E_{e^-})^2 - (\mathbf{p}_{e^+} \cdot c + \mathbf{p}_{e^-} \cdot c)^2} \tag{2.16}$$

where $E_{e^\pm}$ is the total energy, $\mathbf{p}_{e^\pm}$ is the three momenta in the laboratory system and c is the velocity of light. In the relativistic limit, the rest mass of the electron is so small compared to its energy that it is negligible and thus $E_{e^\pm} \approx |\mathbf{p}_{e^\pm}|$ can be used. Consequently, this approach provides to determine the invariant mass using the three momenta $p_{e^\pm}$ of the electrons and their opening angle θ:

$$m_{e^+e^-} = 2 \cdot \sin(\frac{\theta_{e^+e^-}}{2}) \cdot \sqrt{p_{e^+} \cdot p_{e^-}} \tag{2.17}$$

Figure 2.4 illustrates the dielectron spectrum as a function of invariant mass.

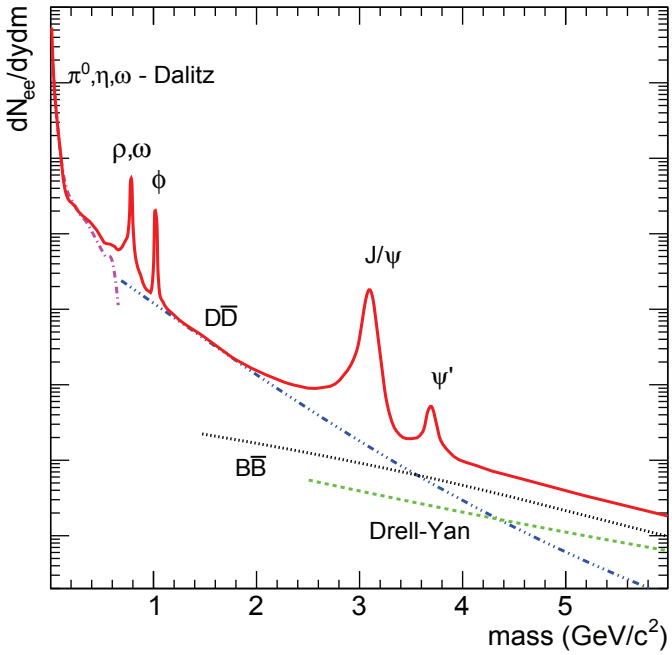

Figure 2.4.: Known dielectron sources as a function of invariant mass [21].

The various contributions to the dielectron spectrum can be associated with different stages of the collision. In the very early collision phase ($\tau \approx 1$ fm/c), dielectrons are produced in hard-scattering processes such as Drell-Yan. The Drell-Yan process is the interaction of a valence-/sea-quark of the nucleon with a sea-antiquark of the other nucleon. These quarks annihilate to form a virtual photon which then decays into an electron-positron pair:

$$q + \bar{q} \rightarrow \gamma^* \rightarrow e^+ + e^-$$

The Drell-Yan process contributes mainly to the high mass region. Another particle which also contributes to the high mass region is J/ψ. The J/ψ production comes mainly from

hard-scattering processes, as well. J/ψ particles produced in the initial stage of the collision are suppressed due to the Debye-like color screening [22] and it is a signature for the presence of the QGP. These dielectron sources from hard-scattering processes in the high mass region allow to study deconfinement effects in hot and dense medium.
Other hard-scattering processes are open charm (D and $\bar{D}$) and beauty (B and $\bar{B}$) meson productions where a quark of the nucleon interacts with an antiquark of the other nucleon by forming a virtual gluon which converts into $c\bar{c}/b\bar{b}$ pair:

$$q + \bar{q} \rightarrow g^* \rightarrow c + \bar{c} \ (\ or\ b + \bar{b})$$

A $c\bar{c}$ (or $b\bar{b}$) can also be produced by the gluon-gluon interaction:

$$g + \bar{g} \rightarrow c + \bar{c} \ (\ or\ b + \bar{b})$$

An open charm meson D consists of a charm quark (c) and a light antiquark ($\bar{u}$, $\bar{d}$ or $\bar{s}$). In contrast, the corresponding antiparticle $\bar{D}$ meson is composed of an anticharm quark ($\bar{c}$) and a light quark (u, d or s). Similarly to the open charm meson, the compositions of constituents for an open beauty meson B and its corresponding antiparticle $\bar{B}$ are the following: $B = b + \bar{q}$ ($\bar{u}$, $\bar{d}$ or $\bar{s}$) and $\bar{B} = \bar{b} + q$ (u, d or s). The open charm and beauty mesons can decay into an electron and another particle (e.g. for the open charm meson $D^- \rightarrow e^- + X$, $D^+ \rightarrow e^+ + X$) forming an electron-positron pair and they finally create the so-called $c\bar{c}$ and $b\bar{b}$ continuum. The $D\bar{D}$ and $B\bar{B}$ mesons are dominating dielectron sources in the intermediate mass region and allow to study in-medium properties and thermal radiation of the QGP.
While the QGP cools down below the transition temperature ($\tau < 10$ fm/c) and converts into a hot hadron gas, dielectrons are preferentially emitted by the annihilation of pions/kaons and by the scattering between other hadrons. The two-body annihilation processes are dynamically enhanced through the formation of light vector meson resonances such as the ρ, ω and ϕ mesons which can decay into e^+e^- pairs. The invariant mass of the e^+e^- pairs corresponds to the mass distribution of the light vector mesons at the moment of decay. Therefore, the ρ, ω and ϕ mesons are interesting to investigate their in-medium modifications and play an important role in heavy-ion physics. Here, the ρ meson is of particular interest for the study of in-medium properties due to its very short lifetime (τ = 1.3 fm/c) compared to lifetime of the fireball and it has a broader decay width than those of the ω and ϕ mesons. Figure 2.5 illustrates the dielectron invariant mass spectrum in Pb-Au collisions at 158 AGeV measured by the CERES experiment at the SPS. The measurements are compared to dielectron cocktail simulations, which consider the vacuum contributions as depicted in Figure 2.5 (a), and in-medium modifications as depicted in Figure 2.5 (b). In Figure 2.5 (b), the first model indicated by the blue line is based on the dropping ρ mass scenario [23] and the second model indicated with the red line is based on the in-medium broadening of the vector spectral function [5]. As it can be clearly seen, the second model agrees better with the data [1, 5].
After freeze-out (after $\tau \approx$ 10-12 fm/c), dielectrons are emitted by the Dalitz decays of light mesons (π^0, η, η', ω and ϕ) which are long-lived. These dielectron sources do not contain any information on in-medium properties [5, 24].
This sorting of the dielectron spectrum according to the collision phases above can allow us to group the invariant mass spectrum (Figure 2.4) into three mass regions. The high mass region (HMR, $m_{ee} > 3$ GeV/c^2) includes the Drell-Yan process, J/ψ and ψ' resonances. The intermediate mass region (IMR, $1.1 < m_{ee} < 3$ GeV/c^2) is dominated by the

semileptonic decays of the open charm and beauty mesons. Finally, in the low mass region (LMR, $m_{ee} < 1.1$ GeV/c^2), dielectrons are emitted by the Dalitz decays of the π^0, η, η', ω, ϕ and resonance decays of the ρ, ω, ϕ mesons.

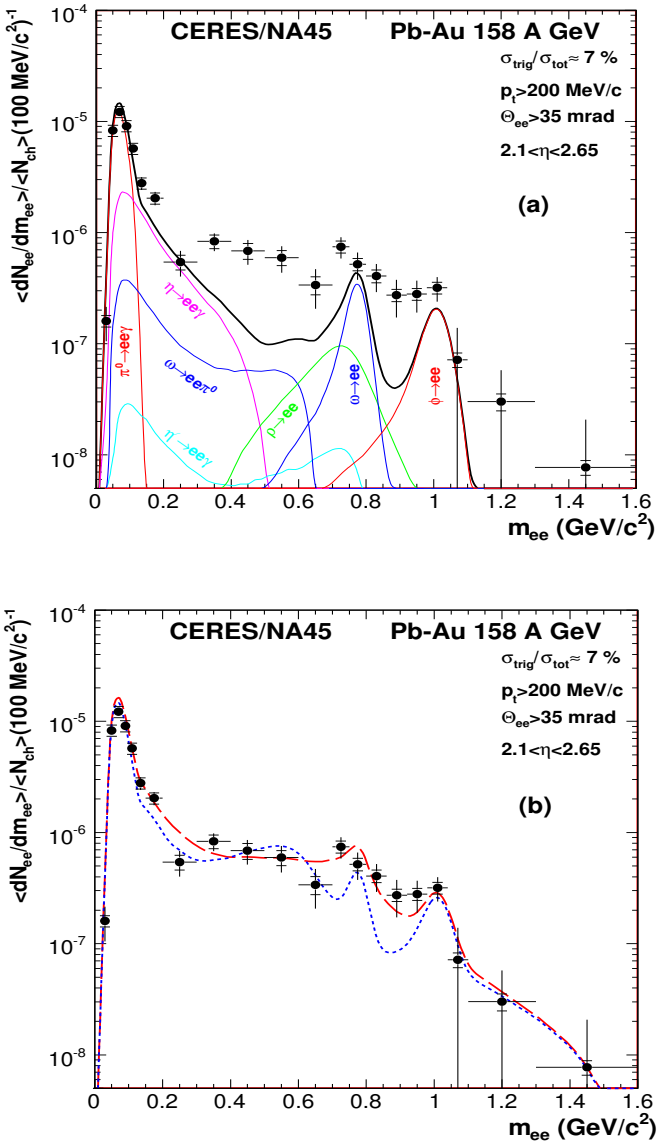

Figure 2.5.: a: The invariant e^+e^- mass spectrum measured by the CERES experiment at the SPS and compared to the expectation from hadronic decays. b: The same data compared to calculations including a dropping ρ mass (blue) and a broadened ρ-spectral function (red) [25].

2.6. A Large Ion Collider Experiment (ALICE)

ALICE [26] is a heavy-ion detector located at CERN and one of the experiments at the LHC. It is designed to study strongly interacting matter and the QGP at extreme high temperature and energy density in Pb–Pb collisions. The physics program of ALICE also includes p–Pb and pp collisions. p–Pb collisions allow to vary energy density and interaction volume. Data from pp collisions are used as reference data for the heavy-ion programme and complementary for several QCD topics to the other LHC detectors [27]. The schematic layout of the ALICE detector systems is shown in Figure 2.6. The ALICE detector consists of two parts. The forward muon spectrometer is a forward single arm spectrometer to detect muons in the pseudorapidity region of -4.0$<\eta<$-2.5. The central part or *central barrel* measures hadrons, electrons and photons. The central barrel covers the direction perpendicular to the beam in the pseudorapidity region of -0.9$<\eta<$0.9 and it is located inside a solenoid magnet which provides a uniform magnetic field of 0.5 T [27, 28].

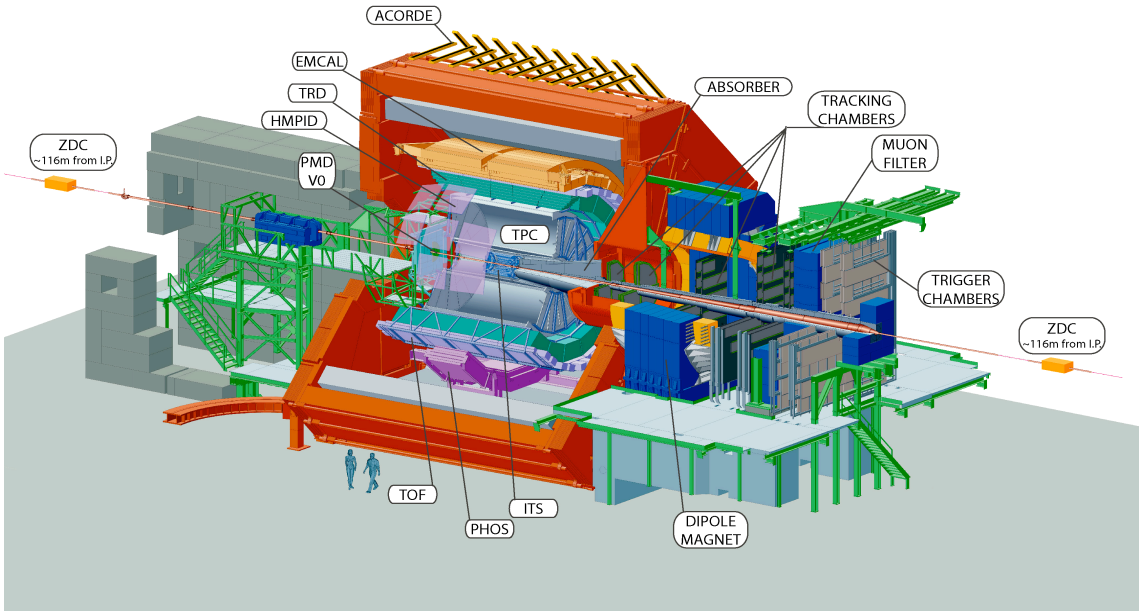

Figure 2.6.: Schematic layout of ALICE.

In the following, the central barrel detectors which are relevant for this dielectron cocktail study are briefly explained from the inner to outer layer.

The Inner Tracking System (ITS) [27, 29] is situated at the innermost of central barrel. It consists of six cylindrical layers of high resolution tracking silicon detectors and covers the pseudorapidity region of $|\eta|<0.9$. The beam pipe is worked radially outwards by the two inner Silicon Pixel Detectors (SPD) covering the region of $|\eta|<1.98$ in the first and $|\eta|<1.4$ in the second layer, two Silicon Drift Detectors (SDD) and two double-sided Silicon Strip Detectors (SSD). The ITS provides primary and secondary vertex information

in the region of high track density close to the primary interaction and it independently identifies particles with low transverse momenta p_{T} via their energy loss measurement ($\mathrm{d}E/\mathrm{d}x$). The four outer layers of the ITS (SSD and SDD) perform this independent Particle IDentification(PID) in the non-relativistic region which provides that the ITS works in the stand-alone mode as a low p_{T} particle spectrometer.

The Time Projection Chamber (TPC) [27, 30] is the main detector for track reconstruction. In order to handle high multiplicities (up to $\mathrm{d}N/\mathrm{d}y \approx 8000$) created in Pb–Pb collisions and to gain most of tracking informations, a large TPC is designed with a cylindrical shape around the beam axis (the length of 5 m, inner radius of approximately 85 cm, outer radius of approximately 2.5 m). It consists of a cylindrical field cage and the read-out chambers at the end-plates. The field cage is filled with a cold gas mixture of Ne(90%) and CO_2(10%). This gas mixture is chosen for the TPC to reach a maximum drift time of $\sim$90 μs. In the field cage, the primary electrons are transported over a distance of up to 2.5 m on either side of the central electrode to the end plates. Through a central high-voltage electrode and two opposite axial potential dividers, the field cage create a uniform electrostatic field. For the signal read-out, Multi-Wire Proportional Chambers (MWPC) at the end-plates are used. Electrons produced by the ionization of the gas molecules are accelerated to the end-plates by electrostatic drift field and measured by the MWPC. In the upgraded TPC, MWPC will be exchanged by Gas Electron Multipliers (GEM) to measure tracks in a collision rate of $\sim$50 kHz in Pb–Pb collisions [31]. The second main task of the TPC is the PID via specific energy loss of electrically charged particles in the gas. Particles such as electrons, pions, kaons, protons, muons and deuterons can be identified by their $\mathrm{d}E/\mathrm{d}x$.

The Transition Radiation Detector (TRD) [27, 32] surrounds the TPC and consists of 540 large area drift chambers with the drift direction perpendicular to the wire planes. The drift chambers are arranged in 18 super-modules, contain 30 modules in 5 longitudinal stack and 6 radial layers. Transition Radiation (TR) is emitted by fast charged particles passing through the radiator with alternating dielectric constants. In the momentum range from 1 to 10 GeV/c, TR is produced only by electrons. Therefore, the TRD provides electron IDentification(eID) in the central barrel for momenta above 1 GeV/c. Moreover, TR from electrons passing the radiator can be used together with the specific energy loss in a suitable gas mixture to obtain the necessary pion rejection capability. For momenta below 1 GeV/c, electrons can be identified via $\mathrm{d}E/\mathrm{d}x$ measurement in the TPC. The TRD covers the central rapidity region ($|\eta|<0.9$), as well.

The Time-Of-Flight Detector (TOF) has a cylindrical shape covering the central rapidity region of $|\eta|<0.9$. It measures the time which takes particles to go through the detector. For the TOF, a gas detector called the Multi-gap Resistive-Plate Chamber(MRPC) is chosen. MRPC has a very good time resolution (60 ps) to differentiate particles with 99.9 % efficiency. It has a modular structure with 18 sectors. Each of these sectors is divided into 5 modules along the beam direction. The modules contain a total of 1638 detector elements (MRPC strips). The TOF is designed for the PID in the intermediate momentum range below about 2.5 GeV/c for pions/kaons and up to 4 GeV/c for protons. Moreover, the TOF together with the ITS and TPC provides event-by-event identification of large samples of pions, kaons, and protons [27].

The Photon Spectrometer (PHOS) is a high-resolution and high-granularity electromagnetic calorimeter to measure photons and neutral mesons. A set of multi-wire chambers in front of the PHOS helps to separate charged particles from photons (Charged Particle Veto - CPV). The PHOS covers a pseudorapidity region of $|\eta| \leq 0.12$ and has a azimuthal acceptance of 100° ($220° < \phi < 320°$) [27].

3. Dielectron cocktail simulation

This chapter is dedicated to cocktail calculation of known dielectron sources in minimum bias pp collisions at $\sqrt{s}$ = 7 TeV, p–Pb collisions at $\sqrt{s_{\rm NN}}$ = 5.02 TeV and in central and semi-central Pb–Pb collisions at $\sqrt{s_{\rm NN}}$ = 2.76 TeV. In this dielectron cocktail study, the calculation of the cocktails in p–Pb and Pb–Pb collisions is based on scaling of events from pp collisions, and therefore, hot/cold nuclear matter effects are not considered.

Since computing and consequently the ALICE offline framework (AliRoot) [33] are fundamental aspects of the dielectron cocktail study, a brief introduction to AliRoot and the classes used for the dielectron cocktail calculation are given in Section 3.1. In the subsequent three sections, the simulation frameworks for event generation and data inputs are presented. In Section 3.2 the Dalitz decays of π^0, η, η', ω, ϕ and dielectron decays of ρ, ω, ϕ in the LMR, in Section 3.3 semileptonic heavy-flavor decays of $D\bar{D}$, $B\bar{B}$ in the IMR and in Section 3.4 dielectron decays of J/ψ in the HMR are discussed. Section 3.4 is followed by the effect of bremsstrahlung on electrons and its implementation for the dielectron cocktail. Finally, in Section 3.5 the calculation of systematic uncertainties on the dielectron cocktail for each collision system is presented.

In ALICE, electrons are identified in the central barrel at mid-rapidity, $|\eta^e|$<0.8, due to their specific energy loss dE/dx in the TPC and ITS, and the time-of-flight signal in the TOF detector. Thus, the rapidity cut of $|\eta^e|$<0.8 is applied while simulating dielectron cocktail. Another kinematical cut is applied on the transverse momentum $p_{\rm T}^e$. For the dielectron cocktail in pp collisions, $p_{\rm T}^e$>0.2 GeV/c is required. In Pb–Pb collisions, the required cut is $p_{\rm T}^e$>0.4 GeV/c. In case of p–Pb collisions, dielectron cocktails are generated for both $p_{\rm T}^e$>0.2 and 0.4 GeV/c, respectively.

3.1. ALICE offline framework (AliRoot)

AliRoot is the ALICE offline framework developed at CERN, based on ROOT [34] which is an object-oriented software based on the programming language C++, and used for physics analysis, simulation and reconstruction of events. As a simulation framework, AliRoot provides an interface to *external event generators* such as PYTHIA [35] and to *internal event generators* which allow to generate events employing parametrized pseudorapidity and transverse momentum distributions that are provided by the user. The user-defined parametrizations are stored in libraries.
The *AliGenerator* class is the base class to delegate the task to an external generator using the *TGenerator* interface. The *AliGenParam* class is an abstract internal generator interface to connect independent parametrization libraries. To combine these different generators is the task of the *AliGenCocktail* class. In Figure 3.1 the above mentioned classes are schematically illustrated, and classes used for the dielectron cocktail simulation in the LMR are chosen as example, i.e. *AliGenEMlib* and *AliGenEMCocktail* where *EM* stands for electromagnetic.

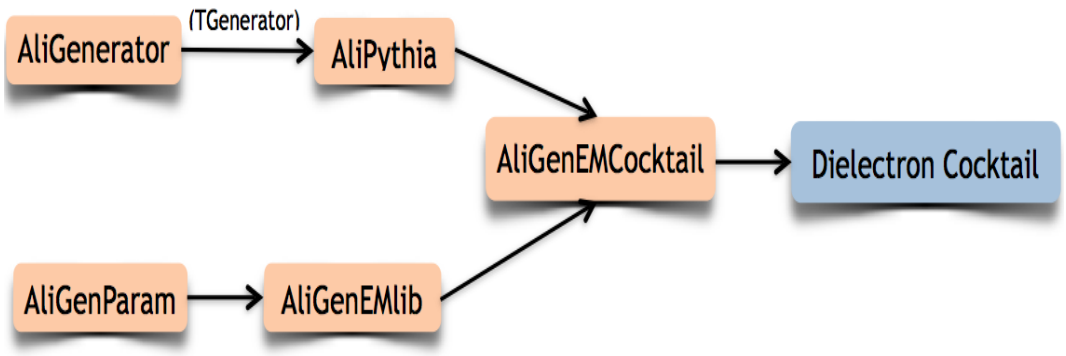

Figure 3.1.: Illustration of the AliRoot classes for dielectron cocktail simulation in the LMR.

3.2. Low mass region

3.2.1. External event generator

The dielectron cocktail components in the LMR are simulated with a new hybrid event generator which has been developed within this work. It is based on PYHTIA and EXODUS [36] the latter being an event generator developed by PHENIX [37]. The reason behind creating a combined event generator was the fact that PYTHIA does not correctly describe the line shapes of resonances and Dalitz decays. However, they can be described by EXODUS quite reasonably. For this purpose, the EXODUS code is adapted to AliRoot and PYTHIA. As a result of this, a new class called *AliDecayerExodus* [1] is developed and committed into AliRoot. Furthermore, the *AliDecayerExodus* class has an advantage because of EXODUS coding and it is that users have full control over decay implementations. It enables us to simply update and modify properties such as form factors or decay functions in the class.

In this new dielectron cocktail framework, decay kinematics are implemented by EXODUS. The Dalitz decays of π^0, η, η', ω and ϕ [2] are treated using the Kroll-Wada function [38] and the measured electromagnetic transition form factors are taken from the Lepton-G data [39]. The line shapes of the ρ, ω and ϕ resonances are defined using the Gounaris-Sakurai function [40]. Figure 3.2 shows the natural line shapes of the Dalitz and resonance decays described by the Kroll-Wada function and the Gounaris-Sakurai function, respectively.
Other tasks for event generation such as decay selections and applying branching ratios (BR) are performed by PYTHIA. Briefly, for the dielectron cocktail calculation in the LMR, the PYTHIA decay table is used and then the particle decay kinematics from PYTHIA are replaced by those from EXODUS. Like PYTHIA, this new hybrid framework developed for the dielectron cocktail produces events only for pp collisions. Then, the internal event

[1] The AliDecayerExodus class is located in the EVGEN directory of AliRoot (AliRoot/EVGEN).
[2] The Dalitz decay of ϕ is switched off in the PYTHIA decay table. Therefore, the ϕ Dalitz decay channel into dielectrons has been switched on at first and then its decay kinematics using the Kroll-Wada function has been added into the *AliDecayerExodus*.

generator to be discussed in Section 3.2.2 is responsible to generate events for all required collision systems by using the corresponding input p_{T}-spectra.

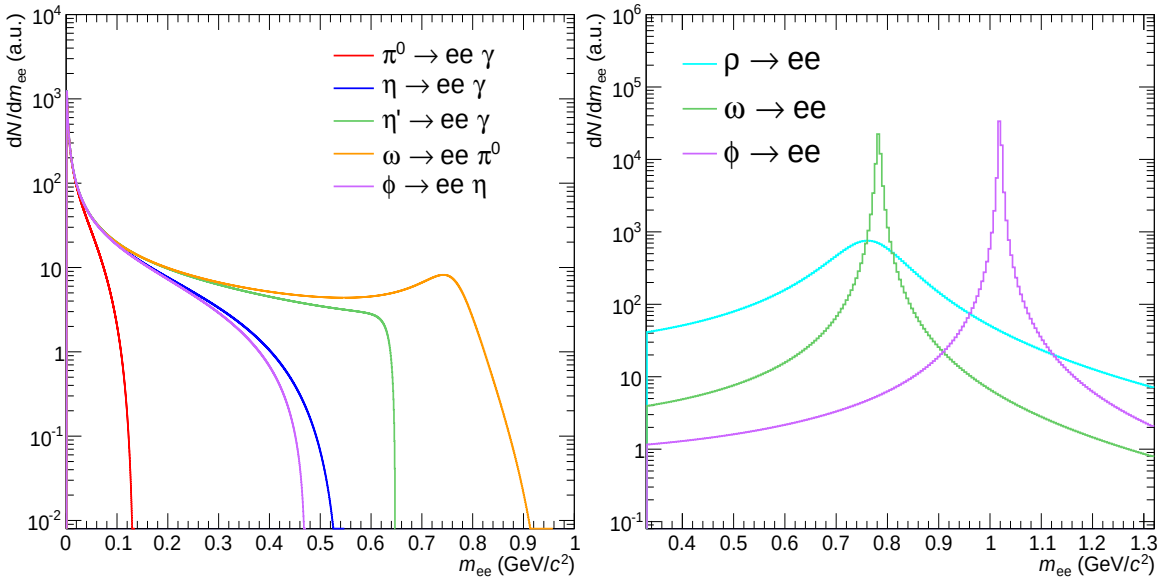

Figure 3.2.: Natural line shapes of the Dalitz(left) and resonance(right) decays described by the Kroll-Wada function and the Gounaris-Sakurai function, respectively.

3.2.2. Internal event generator and inputs

The dominating electron source is $\pi^0(\pi^{\pm})$ due to its high abundance and large branching ratio compared to other mesons. The p_{T} distributions of π^0 and $\pi^{\pm}$ therefore serve as main input for cocktail generation. In order to extract parametrizations of pion p_{T}-spectra in various collision systems, p_{T} distributions measured in ALICE are fitted with corresponding functions. Afterwards, the extracted parameters are collected in the *AliGenEMlib* [3] class which is a user defined parametrization library for electromagnetic probes as mentioned in Section 3.1. Subsequently, the abstract internal generator interface, i.e. the *AliGenParam* class, uses inputs from the *AliGenEMlib* class to generate cocktails in different collision systems.

As cocktail input in pp collisions at $\sqrt{s} = 7$ TeV, the measured p_{T}-spectrum of η is available in addition to the p_{T}-spectrum of π^0 [41]. Therefore, two p_{T}-spectra serve as input in this collision system. Figures 3.3 and 3.4 show p_{T}-differential cross sections of π^0 and η which are measured using PHOS+PCM [4] and fitted with the Tsallis function [43]:

[3] Within this cocktail study, the first step of working with the AliGenEMlib was to modify codes of the AliGenEMlib in favor of users, so that users do not need to compile AliRoot after each switching between parametrizations as before. Now, parameters can be chosen in the so-called fast simulation macro fastGen.C.

[4] PHOS+PCM method [42] is a combined method to measure neutral pions and etas using PHOS (Photon Spectrometer): $\pi^0 \to \gamma\gamma$ and $\eta \to \gamma\gamma$ and PCM (Photon Conversion Method): $\pi^0 \to \gamma\gamma \to \to e^+e^-\ e^+e^-$ and $\eta \to \gamma\gamma \to e^+e^-\ e^+e^-$

$$\frac{\mathrm{d}^2\sigma}{\mathrm{d}y\mathrm{d}p_\mathrm{T}} = c \times \frac{(n-1)(n-2)}{nT \times [nT + m(n-2)]} \times (1 + \frac{m_\mathrm{T} - m}{nT})^{-n} \tag{3.1}$$

where m and m_T denote the particle mass and transverse mass with $m_\mathrm{T} = \sqrt{m^2 + p_\mathrm{T}^2}$, and c, n and T are the free parameters. It can be clearly seen that the Tsallis function with the corresponding parameters for each particle can describe π^0 and η data quite reasonable, so data and fit agree well.

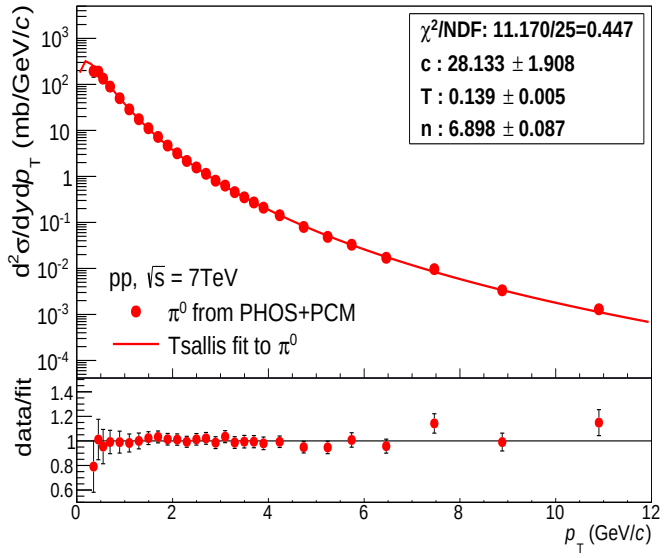

Figure 3.3.: Measured p_T-differential cross section of π^0 in pp collisions at $\sqrt{s} = 7$ TeV.

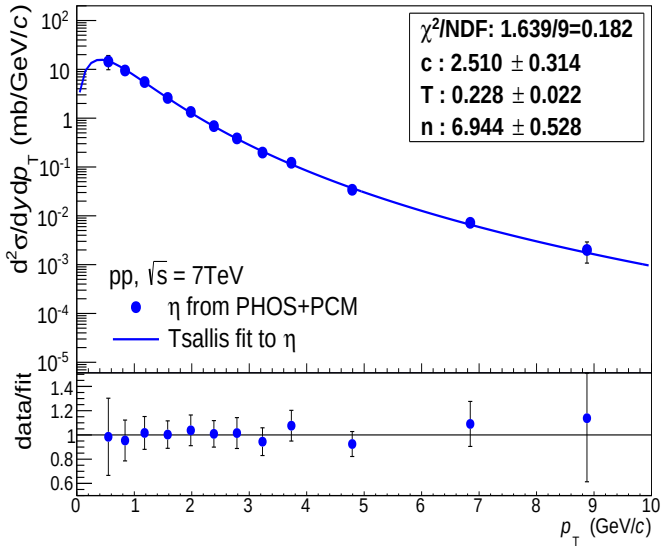

Figure 3.4.: Measured p_T-differential cross section of η in pp collisions at $\sqrt{s} = 7$ TeV.

In minimum bias p–Pb collisions at $\sqrt{s_{\mathrm{NN}}} = 5.02$ TeV, the p_{T}-spectra of $(\pi^+ + \pi^-)/2$ used as approximation of π^0 serve as cocktail input. The determination of pion input in this collision system is performed by fitting measured p_{T}-differential yields of $\pi^{\pm}$ [44] using the modified Hagedorn exponential function [45] with an additional term $(\frac{p_{\mathrm{T}}}{p_1})^d$:

$$\frac{\mathrm{d}^2N}{\mathrm{d}y\mathrm{d}p_{\mathrm{T}}} = c \times (e^{(a \times p_{\mathrm{T}} - b \times p_{\mathrm{T}}^2)} + \frac{p_{\mathrm{T}}}{p_0} + (\frac{p_{\mathrm{T}}}{p_1})^d)^{-n} \tag{3.2}$$

where c, a, b, p_0, p_1, d and n are the free parameters of the fit function.
p_{T}-differential yields of π^+ and π^- are measured via TPC+TOF up to 2.5 GeV/c and via only TPC from 2.5 up to 20 GeV/c. As it is recognizable in Figure 3.5, $\pi^{\pm}$ can be measured down to very low p_{T} with TPC+TOF.

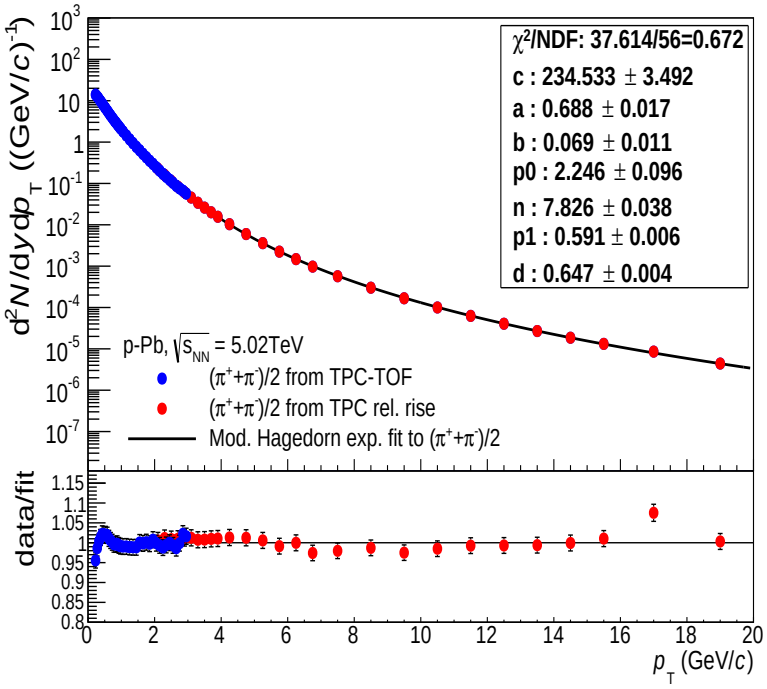

Figure 3.5.: Measured p_{T}-differential yields of $\pi^{\pm}$ (as approximation of π^0) in p–Pb collisions at $\sqrt{s_{\mathrm{NN}}} = 5.02$ TeV.

Figure 3.5 indicates a good agreement between data and fit, and these $\pi^{\pm}$ parametrizations are added into the *AliGenEMlib* as new cocktail input. Next step on p–Pb inputs will be to update the library by adding parametrizations for measured p_{T}-spectra of π^0.

Available cocktail inputs in central (0-10%) and semi-central (20-50%) Pb–Pb collisions at $\sqrt{s_{\mathrm{NN}}} = 2.76$ TeV are both neutral and charged pions. For the dielectron cocktail in central Pb–Pb collisions, the π^0 spectrum is the main cocktail input and the p_{T}-differential yield of π^0 [46] measured with PCM is fitted with the modified Hagedorn exponential function:

$$\frac{\mathrm{d}^2N}{\mathrm{d}y\mathrm{d}p_{\mathrm{T}}} = c \times (e^{(-a \times p_{\mathrm{T}} - |b| \times p_{\mathrm{T}}^2)} + \frac{p_{\mathrm{T}}}{p_0})^{-n} \tag{3.3}$$

where c, a, b, p_0 and n are the free parameters of the fit function and which indicates a good agreement with data as shown in Figure 3.6.

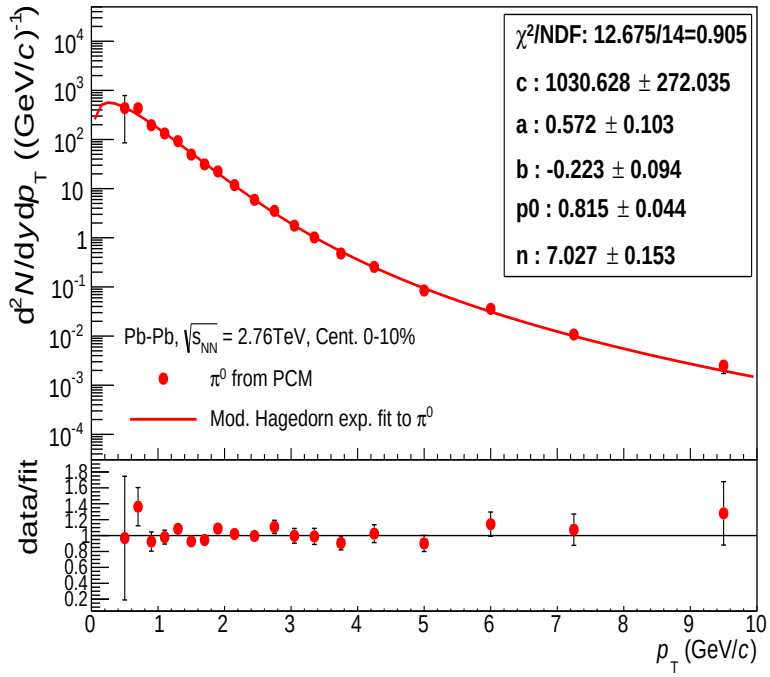

Figure 3.6.: Measured p_{T}-differential yield of π^0 in Pb–Pb collisions at $\sqrt{s_{\mathrm{NN}}} = 2.76$ TeV.

The parametrizations of π^0-spectra in Pb–Pb collisions are added into the *AliGenEMlib* as new inputs for the following centralities: 0-5, 0-10, 10-20, 0-20, 20-40, 0-40, 40-80 and 20-80 %. Besides these new parametrizations for π^0, the published $\pi^{\pm}$ inputs in Pb-Pb collisions [47] have been already existing in the *AliGenEMlib* for the following centralities: 0-5, 5-10, 0-10, 10-20, 20-30, 30-40, 40-50, 50-60, 0-20, 20-40, 40-60 and 0-40 %. Herewith, it is possible to produce required cocktails in Pb–Pb collisions for several centralities.

The cocktail input in semi-central Pb–Pb collisions is obtained by combining pion inputs from different centralities [5], since there is no measured pion p_{T}-spectra for the centrality of 20-50%. With current parametrizations in the *AliGenEMlib*, it is possible to achieve the centrality of 20-50% using only $\pi^{\pm}$ inputs. Therefore, to determine cocktail input in semi-central Pb–Pb collisions, the p_{T}-spectra of $\pi^{\pm}$ [47] measured up to 3 GeV/c via TPC+TOF are used. In order to extract fit parameters, the p_{T}-spectrum of $(\pi^+ + \pi^-)/2$ used as approximation of π^0 is fitted by the modified Hagedorn exponential function (Equation 3.3). The p_{T}-spectrum is shown in Figure 3.7 and one can see a good agreement between data and fit.

[5] Possible combinations with existing $\pi^{\pm}$ inputs are:

$\frac{dN}{dy}(20\text{-}50\%) = [\frac{dN}{dy}(20\text{-}30\%) + \frac{dN}{dy}(30\text{-}40\%) + \frac{dN}{dy}(40\text{-}50\%)] \times \frac{1}{3}$ or

$\frac{dN}{dy}(20\text{-}50\%) = [\frac{dN}{dy}(20\text{-}40\%) \times 2 + \frac{dN}{dy}(40\text{-}50\%)] \times \frac{1}{3}$

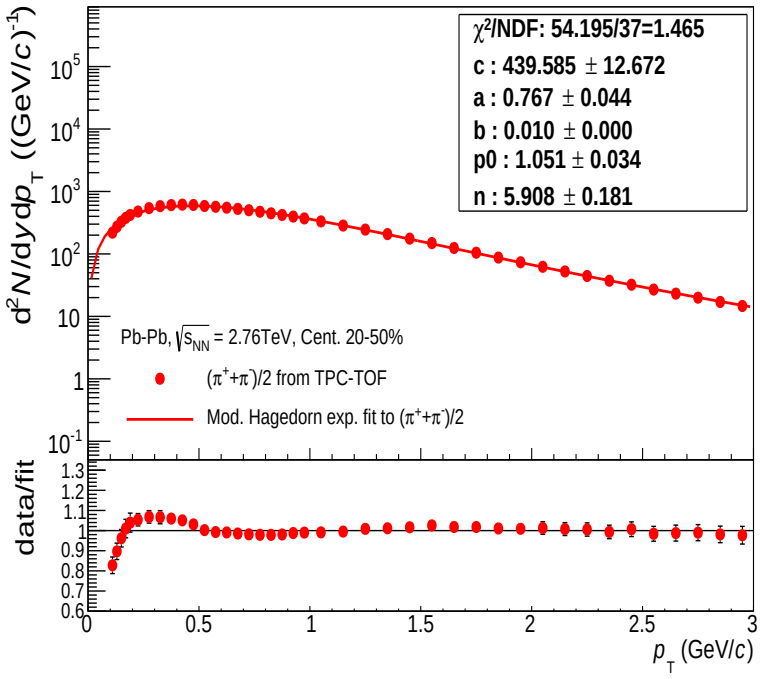

Figure 3.7.: Measured p_{T}-differential yields of $\pi^{\pm}$ (as approximation of π^0) in Pb–Pb collisions at $\sqrt{s_{\mathrm{NN}}} = 2.76$ TeV.

p_T-spectra of the other light mesons (η [6], η', ρ, ω, ϕ) are parametrized using transverse mass scaling (m_{T}-*scaling*) of pion spectra. The m_{T}-*scaling* is applied by fixing all free parameters in the fit function and by replacing the pion's p_{T} by:

$$p_{\mathrm{T}} \rightarrow \sqrt{p_{\mathrm{T}}^2 - m_{\pi^0}^2 + m_{\mathrm{meson}}^2}$$

Afterwards, the absolute normalization of each meson is provided using meson-to-pion ratios as given in Table 3.1.

Meson	Meson/π^0
η	0.48±0.1 [48]
ρ	1.0±0.3 [35]
ω	0.85±0.225 [49]
ϕ	0.4±0.12 [35]
η'	0.25±0.75 [50]

Table 3.1.: Meson to π^0 ratios

[6] Since the p_{T}-differential cross section of η is measured only in pp collisions, m_{T}-scaling of pion spectra is used for η inputs in p–Pb and Pb–Pb collisions.

3.3. Intermediate mass region

3.3.1. External event generator

Contributions of the semileptonic heavy-flavor decays which dominate the IMR are simulated using PYTHIA. To calculate the cross sections of heavy quarks in strong interactions, **M**angano, **N**ason and **R**idolfi (MNR) [51] have developed a next-to-leading-order (NLO) perturbative QCD (pQCD) calculation framework. In order to simulate semileptonic heavy-flavor decays in a reasonable agreement with NLO pQCD calculations, the PYTHIA MNR framework is used and CTEQ6m [52] serves as the parton density function (PDF) for the MNR calculations.

3.3.2. Inputs

Resulting distributions from the PYTHIA MNR framework are normalized by cross sections measured in ALICE. In Table 3.2 and 3.3 the measured $c\bar{c}$ and $b\bar{b}$ cross sections are listed for pp collisions at $\sqrt{s}$ = 2.76 and 7 TeV.

$\sigma_{c\bar{c}}$(2.76 TeV)	4.8 ±0.8(stat.)+1.0(syst.)±0.06(BR)±0.1(FF.)±0.1(lum.)+2.6(extr.) mb
$\sigma_{c\bar{c}}$(7 TeV)	8.5 ±0.5(stat.)+1.0(syst.)±0.1(BR)±0.2(FF.)±0.3(lum.)+5.0(extr.) mb

Table 3.2.: Charm cross sections measured in ALICE in pp collisions at $\sqrt{s}$ = 2.76 and 7 TeV [53].

$\sigma_{b\bar{b}}$(2.76 TeV)	130 ± 15.1(stat) + 42.1(sys) + 3.4(extr) ± 2.5(norm) ± 4.4(BR) μb
$\sigma_{b\bar{b}}$(7 TeV)	281 ± 34(stat) + 53(sys) + 7(extr) μb

Table 3.3.: Beauty cross sections measured in ALICE in pp collisions at $\sqrt{s}$ = 2.76 [54] and 7 TeV [55].

Since there is no pp data at $\sqrt{s}$ = 5.02 TeV, the cross sections of $c\bar{c}$ and $b\bar{b}$ at 5.02 TeV are estimated according to FONLL (Fixed Order + Next-to-Leading Log) calculations [56, 57]. Figure 3.8 shows the measured cross sections of $c\bar{c}$ and $b\bar{b}$ from different experiments as a function of collision energy. Also FONLL predictions are shown for comparison. To estimate the cross sections of $c\bar{c}$ and $b\bar{b}$ at 5.02 TeV, the following ratios given by FONLL calculations are used:

$$\sigma_{c\bar{c}}^{FONLL}(5.02\text{ TeV})/\sigma_{c\bar{c}}^{\text{FONLL}}(7\text{ TeV}) = 0.789 \tag{3.4}$$

$$\sigma_{c\bar{c}}^{FONLL}(5.02\text{ TeV})/\sigma_{c\bar{c}}^{\text{FONLL}}(2.76\text{ TeV}) = 1.561 \tag{3.5}$$

$$\sigma_{b\bar{b}}^{FONLL}(5.02\text{ TeV})/\sigma_{b\bar{b}}^{\text{FONLL}}(7\text{ TeV}) = 0.75 \tag{3.6}$$

According to the ratios in Equations 3.4/3.5 and 3.6, the charm and beauty cross sections at $\sqrt{s}$ = 5.02 TeV are extracted and they are estimated as $\sigma_{c\bar{c}}$ = 6.9 mb and $\sigma_{b\bar{b}}$ = 210 μb. In addition to that, systematic uncertainties for both $\sigma_{c\bar{c}}$ and $\sigma_{b\bar{b}}$ are assigned by systematic uncertainties of the scaling errors and it is estimated as 20% for each.
Measurements and estimations for the cross sections are discussed for pp collisions so far. Additionally, PYTHIA is an event generator for pp collisions as mentioned in Section 3.2.1.

Thus, another normalization factor must be taken into account to calculate contributions from the semileptonic heavy-flavor decays in p–Pb and Pb–Pb collisions. This factor is the number of binary collisions ($N_{\rm coll}$) which is calculated according to Glauber Modeling [58, 59]:

Collision system	$N_{\rm coll}$
p–Pb (MB)	6.9 [60]
Pb–Pb (20-50%)	419.2 [61]
Pb–Pb (0-10%)	1500.5 [61]

Table 3.4.: Numbers of binary collisions in minimum bias p–Pb, semi-central and central Pb–Pb collisions according to Glauber Model calculations.

Consequently, calculated pp yields at $\sqrt{s}$ = 5.02 and 2.76 TeV are multiplied by the corresponding $N_{\rm coll}$ values to obtain yields in p–Pb and Pb–Pb collisions at $\sqrt{s}$ = 5.02 and 2.76 TeV, respectively, for required centralities:

$$(\frac{{\rm d}N}{{\rm d}y})^{5.02{\rm TeV}}_{p-Pb} = N_{\rm coll} \times (\frac{{\rm d}N}{{\rm d}y})^{5.02{\rm TeV}}_{pp} \tag{3.7}$$

$$(\frac{{\rm d}N}{{\rm d}y})^{2.76{\rm TeV}}_{p-Pb} = N_{\rm coll} \times (\frac{{\rm d}N}{{\rm d}y})^{2.76{\rm TeV}}_{pp} \tag{3.8}$$

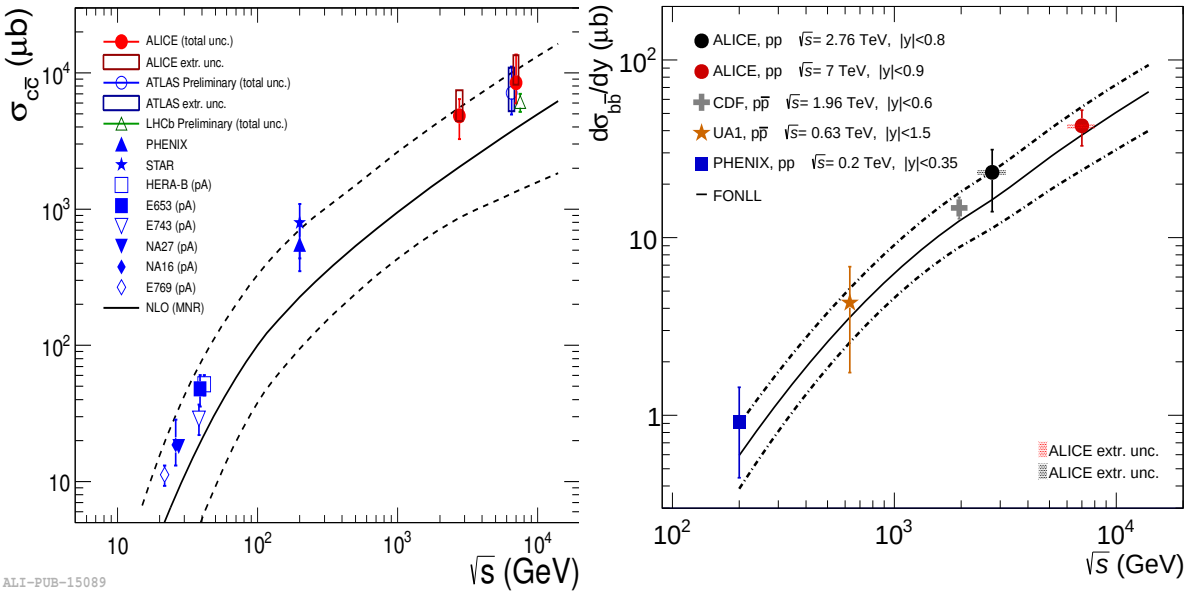

Figure 3.8.: Charm (left) [53] and beauty (right) [54] cross sections from different experiments and FONLL predictions as a function of collision energy.

3.4. High mass region

In the HMR, only dielectrons from the J/ψ particle are included into the dielectron cocktail spectrum. Dielectron contributions of J/ψ are generated with the EvtGen package [62] in AliRoot and the effect of radiative corrections in decays are simulated using PHOTOS [63, 64]. Herewith the radiative decays - known as internal bremsstrahlung - ($J/\psi \rightarrow ee\gamma$) are also considered [7] [65].

In this cocktail study, dielectron decays of J/ψ in pp [66] and p–Pb [67] collisions are taken from the full Monte Carlo (MC) simulation and then they are scaled by the cross sections measured in ALICE (Table 3.5).

$\sigma^{pp}_{J/\psi}$ (7 TeV)	12.4±1.1(stat.)±1.8 (syst.)+1.8(λ_{HE} =1)-2.7(λ_{HE} =-1) μb [68, 65]
$\sigma^{p-Pb}_{J/\psi}$ (5.02 TeV)	367.8 ± 61 nb [69]

Table 3.5.: Production cross sections of J/ψ measured with ALICE in pp and p-Pb collisions at $\sqrt{s}$ = 7 and 5.02 TeV, respectively.

Since statistics for dielectron analysis in Pb–Pb collisions is currently limited, the invariant mass spectrum is being analyzed only up to 0.5 GeV/c^2. Therefore, there is no calculation performed for J/ψ in Pb–Pb collisions for this dielectron study.

3.5. Bremsstrahlung effect and momentum resolution

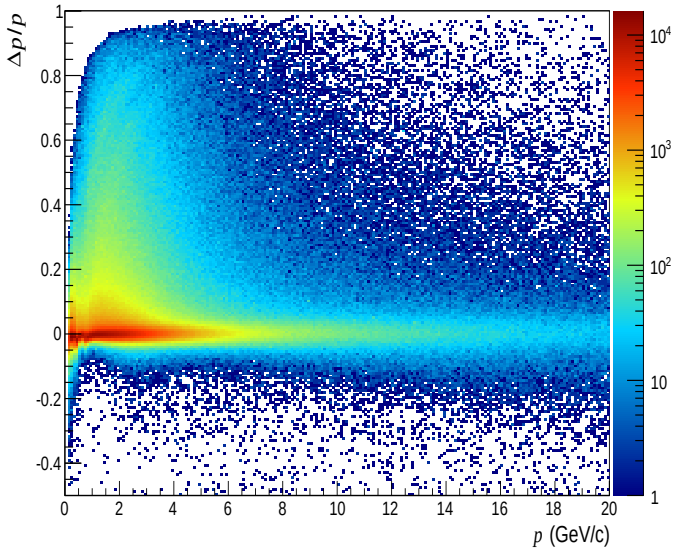

Figure 3.9.: Momentum resolution from full MC detector simulation.

[7] Due to the fact that PYTHIA does not consider the radiative decays of J/ψ, a new framework for decays of J/ψ was previously developed using EvtGen and PHOTOS [65].

Electrons lose a non-negligible part of their energy by interacting with the detector material due to the bremsstrahlung effect. For this reason, the energy loss of electrons in the detector material and its effect on the dielectron cocktail should be taken into account. In order to implement the bremsstrahlung effect, full MC detector simulations from ALICE are used for each collision system separately. To extract the momentum resolution $\Delta p/p$:

$$\frac{\Delta p}{p} = \frac{p_{\text{generated}} - p_{\text{reconstructed}}}{p_{\text{generated}}} \tag{3.9}$$

where $p_{\text{generated}}$ is the momentum of electrons without considering any detector effects and $p_{\text{reconstructed}}$ is the momentum of electrons after all reconstruction and electron identification cuts. Obtained distribution of the momentum resolution $\Delta p/p$ vs. momentum p is stored into a 2D histogram and it is shown in Figure 3.9. Afterwards, slice by slice projections of $\Delta p/p$ are taken for each momentum interval. Figure 3.10 indicates an example of the projection on $\Delta p/p$ for the momentum interval of p = 5.9–6.1 GeV/c. As it can be clearly seen, the distribution of electrons shows a tail on its lower right side which is caused by the bremsstrahlung effect and which means $p_{\text{generated}} > p_{\text{reconstruced}}$. On the other hand, the width of the peaked region is due to momentum resolution.

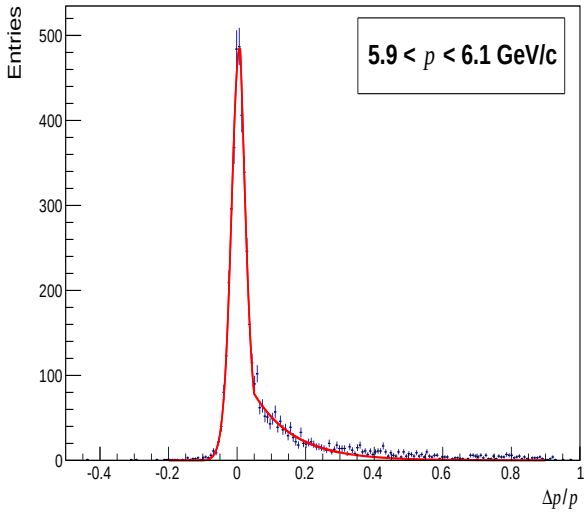

Figure 3.10.: Projection on momentum resolution $\Delta p/p$ for the momentum interval p = 5.9-6.1 GeV/c.

After taking projections for all momentum slices, the obtained 1D histograms of momentum resolution are fitted with a combined function consisting of the Landau function convoluted with the generalized Gaussian [8] and exponential function (Equation 3.10).

$$F_{c_1,\sigma_g,s,k,\sigma_\ell,M_\ell,c_2,\alpha,b}(x) = \begin{cases} c_1 \int G_{\sigma_g,s,k}(x-z) L_{\sigma_\ell,M_\ell}(z) dz & \text{if } x \leq b \\ c_2 exp(-\alpha x) & \text{if } x \geq b \end{cases} \tag{3.10}$$

[8] Compared to the Gaussian, the Generalized Gaussian (GG) has two more variables which are called skewness and kurtosis.

Fitting the peak region with the Landau function convoluted with the generalized Gaussian parametrizes momentum resolution and fitting the tail with the exponential function gives parametrization for the bremsstrahlung effect. Below the border, which is also a parameter, between the Landau+Gaussian and exponential functions (for $x \leq b$), parameters describing the distribution in the peak region are the constant c_1, the width σ_g, skewness s, kurtosis k of the convoluted generalized Gaussian function, the width σ_ℓ and most probable value M_ℓ of the Landau density. For $x \geq b$, the tail is parameterized by the constant c_2 and the slope α of the exponential function. With extracted parameterizations for momentum resolution and the bremsstrahlung tail, the smearing of generated momentum $p_{\text{generated}}$ of electrons is performed and finally their invariant masses are recalculated [70].

Figure 3.11 shows two dielectron cocktail spectra in order to see the effect of bremsstrahlung on the dielectron cocktail [9]. The left panel indicates dielectron cocktail without smearing while the right panel shows dielectron cocktail with smearing. From the dielectron cocktail on the right panel, one can simply recognize smearing due to the bremsstrahlung effect, in particular from the tail of the resonance decay of e.g. ϕ. Also the peak heights of ω and ϕ are decreased after smearing.

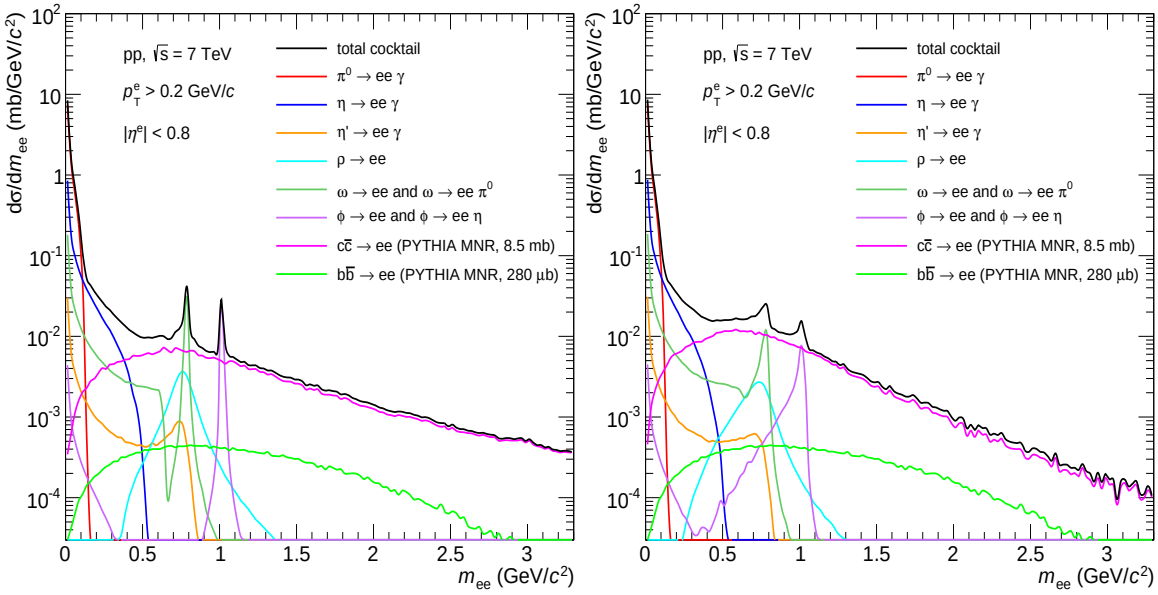

Figure 3.11.: Dielectron cocktails in pp collisions at $\sqrt{s} = 7$ TeV without (left) and with (right) smearing due to the bremsstrahlung effect and momentum resolution.

A comparison of total dielectron cocktails in Figure 3.12 shows the difference better between smeared and unsmeared cases. This indicates that the smearing due to the bremsstrahlung effect and momentum resolution can not be neglected especially for the ω and ϕ resonances, but also towards the HMR.

[9] Since dielectron decays of J/ψ are taken from full MC simulation, the bremsstrahlung effect and momentum resolution have been already taken into account. Thus, the plots present the particle decays except those from J/ψ.

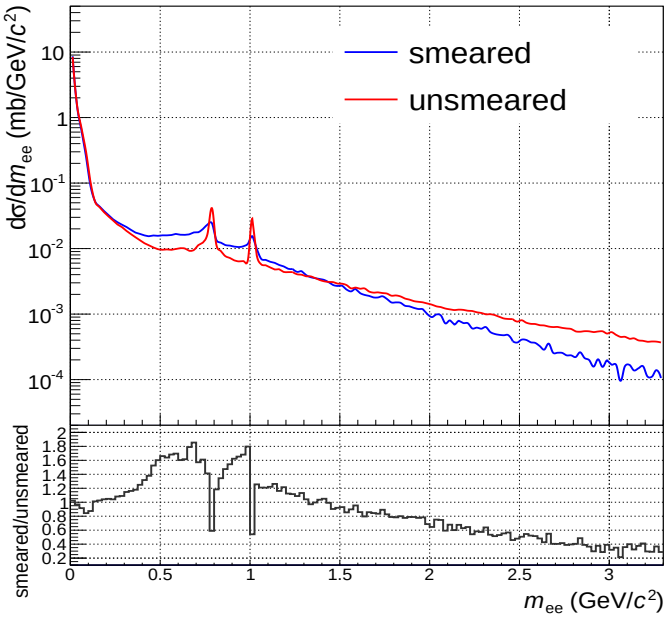

Figure 3.12.: Total dielectron cocktails and their ratios in pp collisions at $\sqrt{s} = 7$ TeV with (blue) and without (red) smearing.

3.6. Calculation of systematic uncertainties

As discussed in Section 3.2.2, the dominating dielectron sources of the cocktail are the pions, and contributions of other mesons in the LMR are derived from pion p_{T}-spectra using m_{T}-*scaling*. Thus, the uncertainty on the pion cross section/yield is the major systematic error source. In order to estimate systematic errors from the pion measurement, pion data are shifted up and down by their systematic uncertainties and re-fitted. Extracted parametrizations from shifted-up and -down pion data are then written into the internal event generator (*AliGenEMlib*), and dielectron cocktails are re-produced from each.
Systematic errors of other light mesons (η, η', ρ, ω and ϕ) are determined by systematic errors on meson-to-pion ratios used for m_{T}-*scaling* given in Table 3.1. Systematic errors of $c\bar{c}$, $b\bar{b}$ and J/ψ are assigned by systematic errors of their measured cross sections given in Tables 3.2, 3.3 and 3.5, respectively. Afterwards, the total systematic error is calculated by adding the individual contributions in quadrature and by averaging upper and lower uncertainties.

Systematic uncertainties on the dielectron cocktail in pp collisions at $\sqrt{s} = 7$ TeV are shown in Figure 3.13 as a function of m_{ee}. For the dielectron cocktail in p–Pb collisions at $\sqrt{s_{\mathrm{NN}}} = 5.02$ TeV, systematic uncertainties are calculated not only as a function of m_{ee} as shown in Figure 3.14 but also as a function of pair p_{T}. Therefore, Figures 3.15 and 3.16 indicate systematic uncertainties as a function of p_{T}^{ee} for the invariant mass slices of m_{ee}<0.14 GeV/c^2, 0.14<m_{ee}<0.75 GeV/c^2, 0.75<m_{ee}<1.1 GeV/c^2 and 1.1<m_{ee}<3.0 GeV/c^2. Finally, systematic uncertainties on the cocktail in central and semi-central Pb–Pb collisions at $\sqrt{s_{\mathrm{NN}}} = 2.76$ TeV are shown in Figure 3.17 as a function of m_{ee}.
It is remarkable that the $c\bar{c}$ contribution has a large uncertainty and therefore it is the dominating error source in particular in the IMR.

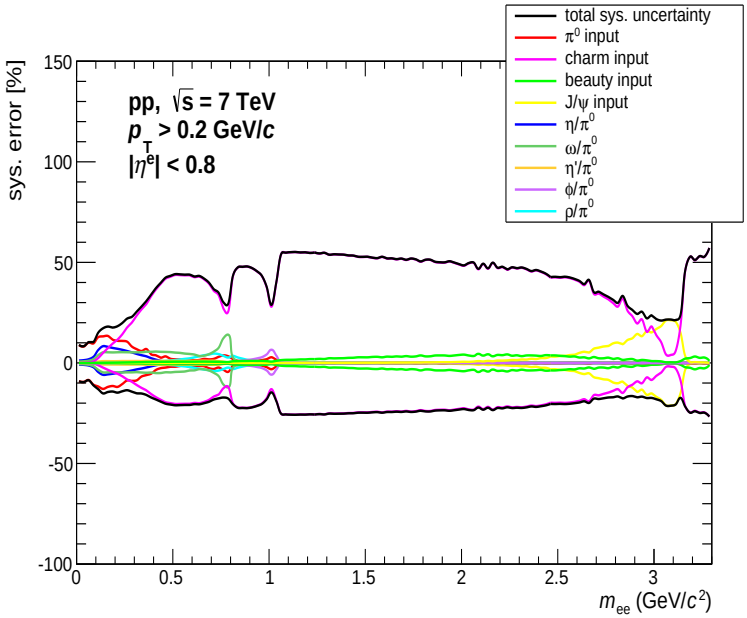

Figure 3.13.: Total and individual systematic uncertainties of dielectron sources as a function of m_{ee} in pp collisions at $\sqrt{s} = 7$ TeV.

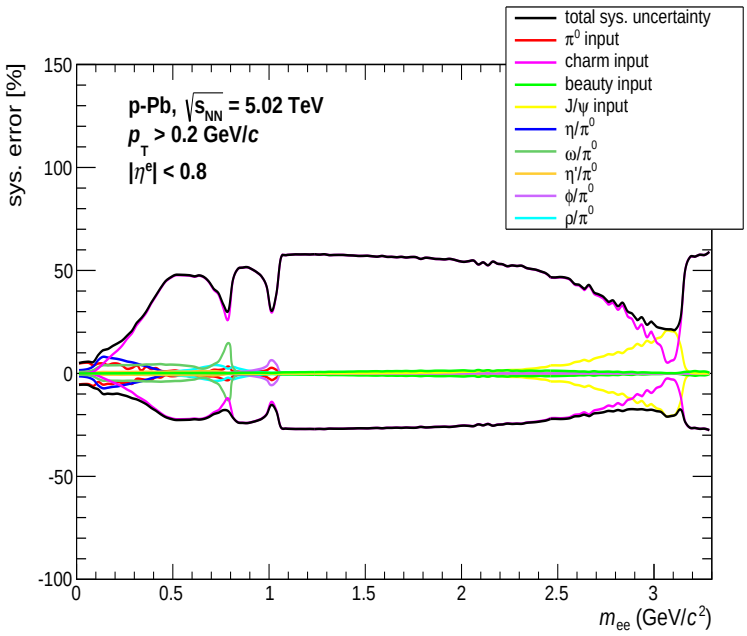

Figure 3.14.: Total and individual systematic uncertainties of dielectron sources as a function of m_{ee} in p–Pb collisions at $\sqrt{s_{\mathrm{NN}}} = 5.02$ TeV.

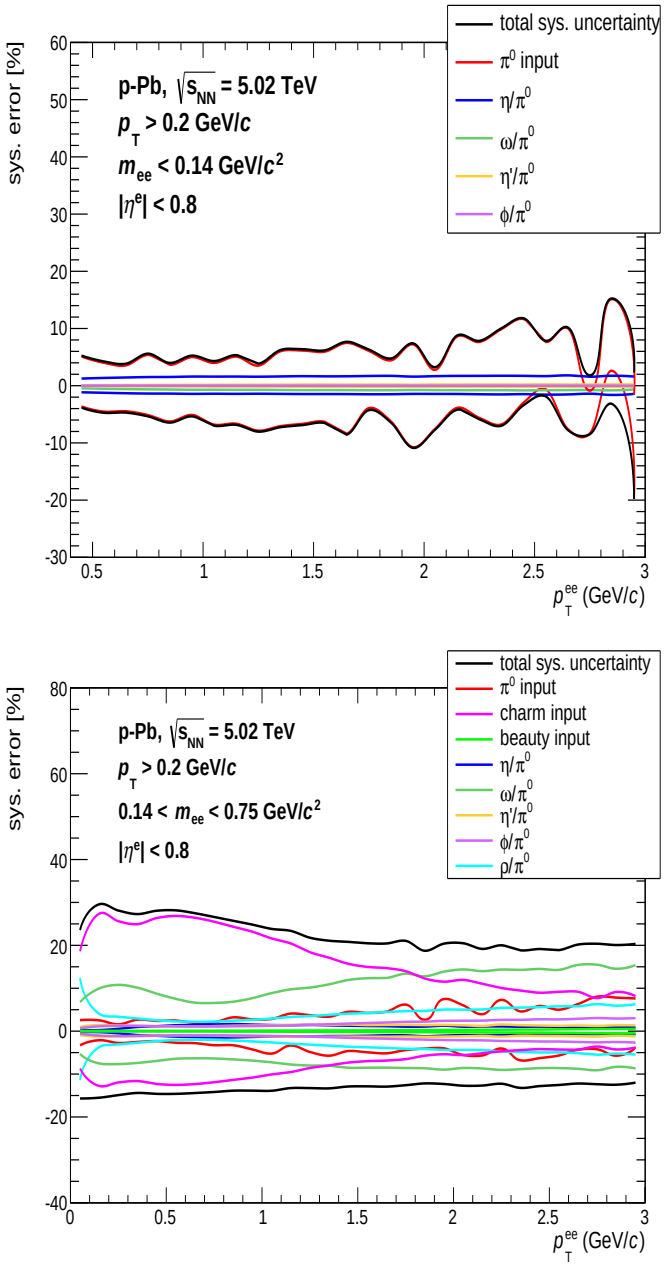

Figure 3.15.: Total and individual systematic uncertainties of dielectron sources as a function of p_{T}^{ee} in p–Pb collisions at $\sqrt{s_{\mathrm{NN}}} = 5.02$ TeV, for $m_{ee} < 0.14$ GeV/c^2 (upper panel) and for $0.14 < m_{ee} < 0.75$ GeV/c^2 (lower panel).

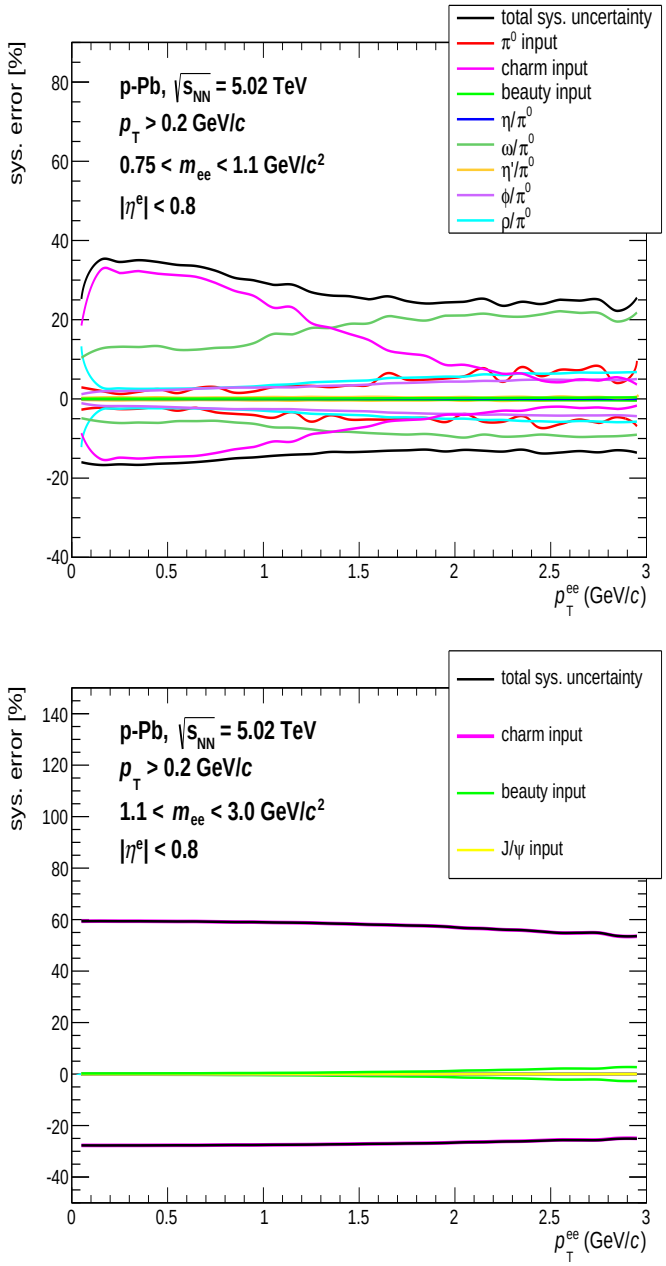

Figure 3.16.: Total and individual systematic uncertainties of dielectron sources as a function of p_{T}^{ee} in p–Pb collisions at $\sqrt{s_{\mathrm{NN}}} = 5.02$ TeV, for $0.75 < m_{ee} < 1.1$ GeV/c^2 (upper panel) and $1.1 < m_{ee} < 3.0$ GeV/c^2 (lower panel).

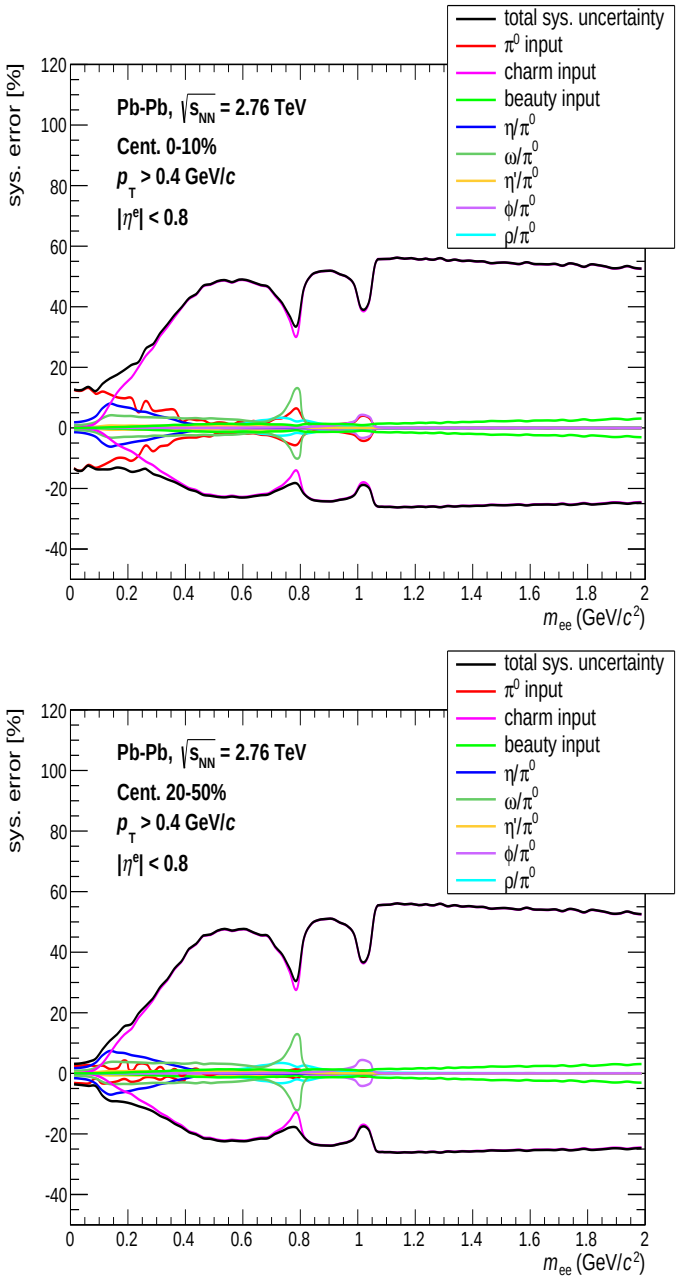

Figure 3.17.: Total and individual systematic uncertainties of dielectron sources as a function of m_{ee} in central (upper panel) and semi-central (lower panel) Pb–Pb collisions at $\sqrt{s_{\mathrm{NN}}} = 2.76$ TeV.

4. Results

In this chapter, dielectron cocktail results compared to data in minimum bias pp collisions at $\sqrt{s}$ = 7 TeV, p–Pb collisions at $\sqrt{s_{\rm NN}}$ = 5.02 TeV, and in central and semi-central Pb–Pb collisions at $\sqrt{s_{\rm NN}}$ = 2.76 TeV are discussed.

4.1. Dielectron cocktail in pp collisions at $\sqrt{s}$ = 7 TeV

Figure 4.1 shows the ALICE preliminary invariant mass spectrum in pp at 7 TeV compared to cocktail calculations which are generated using only EXODUS codes. The invariant mass spectrum is calculated as follows:

$$\frac{1}{N_{evt}}\frac{\mathrm{d}\sigma}{\mathrm{d}m_{\rm ee}} = \frac{1}{N_{evt}}\frac{\mathrm{d}N^{\rm ee}_{\rm corr}}{\mathrm{d}m_{\rm ee}} \times \sigma_{\rm INEL} \tag{4.1}$$

where N_{evt} is the number of events, $\mathrm{d}N^{\rm ee}_{\rm corr}$ is the efficiency corrected number of dielectron pairs and $\sigma_{\rm INEL}$ [71] is the inelastic cross section.

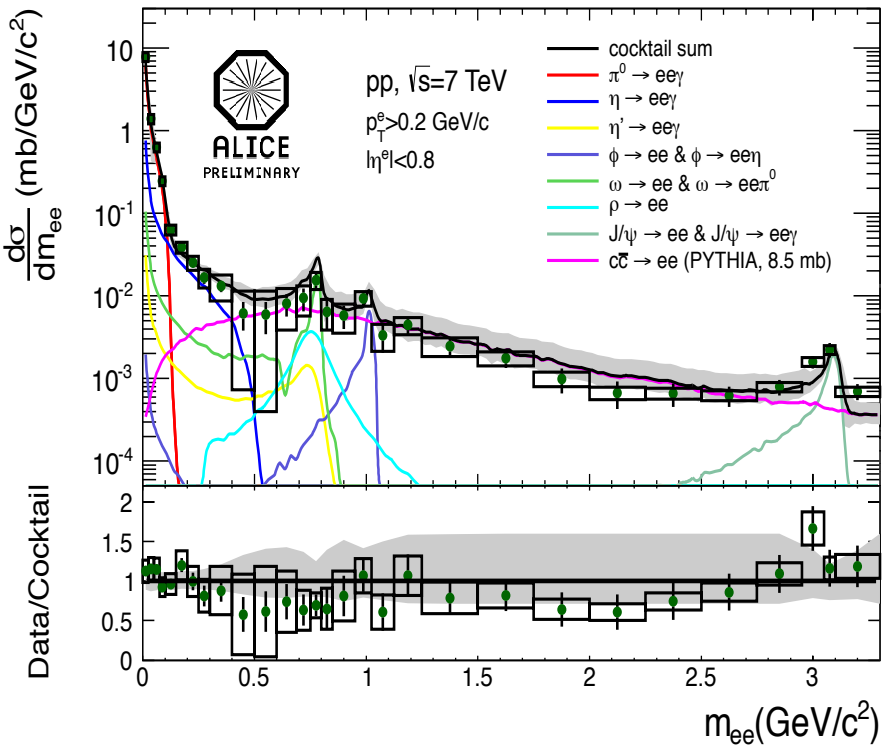

ALI-PREL-43484

Figure 4.1.: Preliminary pp result measured at $\sqrt{s}$ = 7 TeV and comparison of data to previous cocktail calculations from EXODUS [66].

Within this cocktail study, a new hybrid cocktail framework is developed as discussed in Section 3.2.1 and dielectron cocktails are generated with PYTHIA+EXODUS, namely using the *AliDecayerExodus* class. Furthermore, the new dielectron cocktails include two more updates. First, the bremsstrahlung effect (Section 3.5), which was implemented in the old cocktail only for the resonances of ω and ϕ, is applied to all particles. Second, the beauty contribution (Section 3.3) is included in the new cocktail. Finally, the dielectron cocktail is updated accordingly and the new cocktail is compared to the preliminary data points (Figure 4.2).

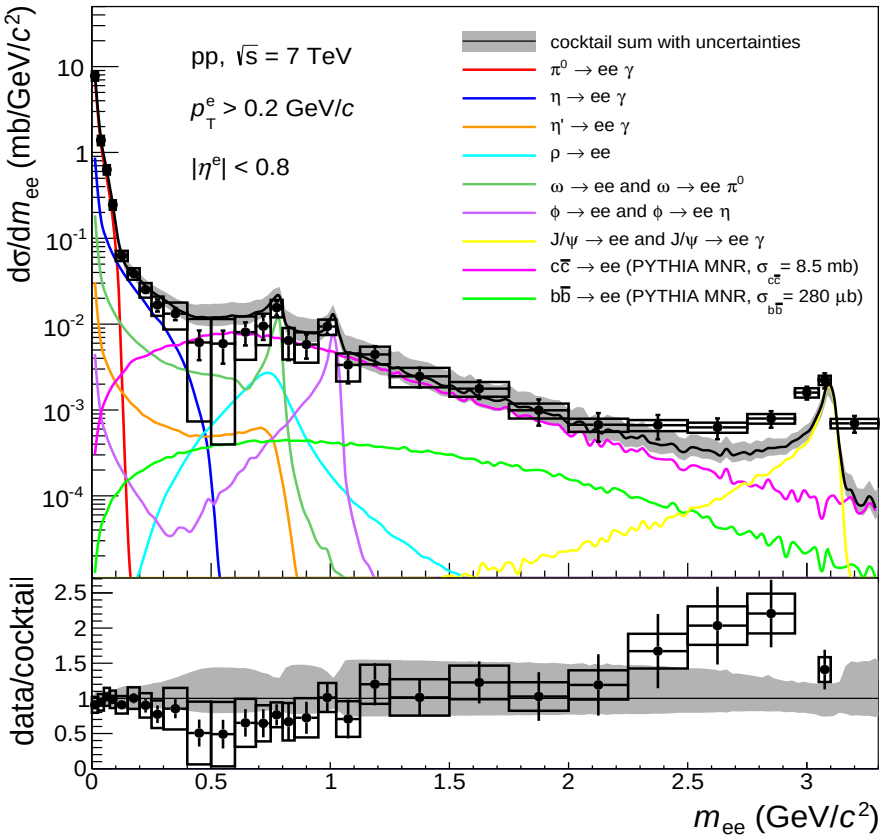

Figure 4.2.: Preliminary invariant mass spectrum compared to the new dielectron cocktail based on PYTHIA and EXODUS.

As one can see, the new cocktail based on PYTHIA+EXODUS and the preliminary data are not in agreement around the J/ψ region, unlike the old dielectron cocktail. On the other hand, the preliminary data are also updated and Figure 4.3 indicates the comparison of the new dielectron cocktail to the current pp result [72] which will be finalized soon. In this comparison, the data and the dielectron cocktail agree better in the IMR and HMR within their systematic uncertainties, however, in the LMR especially around 0.5 GeV/c^2 the data are still below the cocktail.

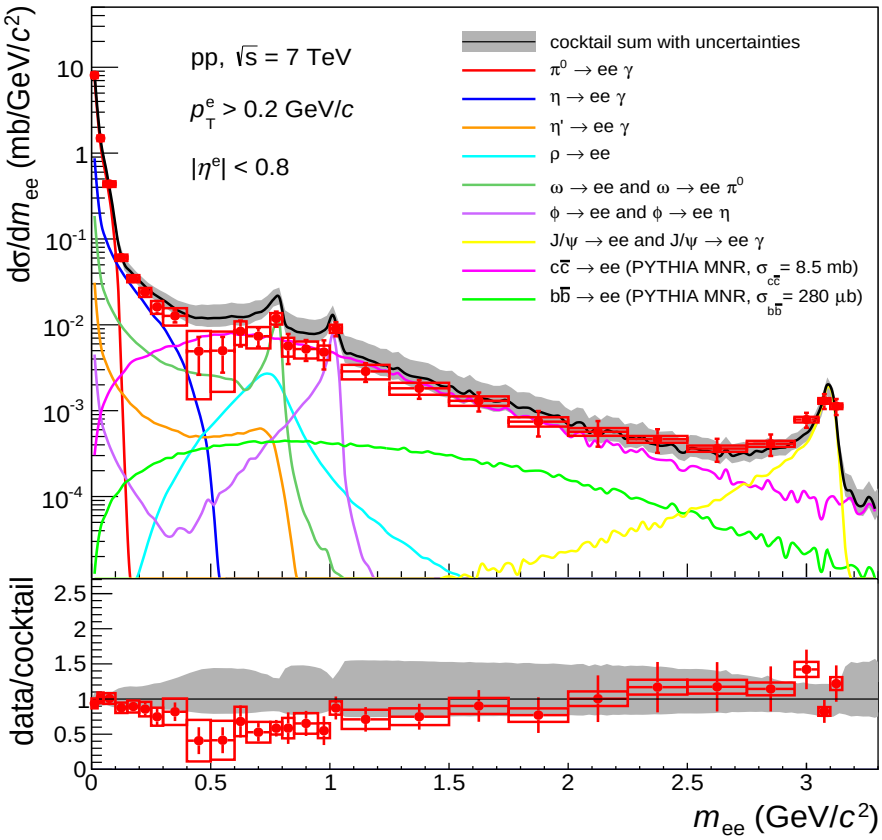

Figure 4.3.: Updated pp data (work in progress) and its comparison to the new dielectron cocktail based on PYTHIA+EXODUS.

4.2. Dielectron cocktail in minimum bias p–Pb collisions at $\sqrt{s_{\mathrm{NN}}}$ = 5.02 TeV

The p–Pb results are performed for two different single leg p_{T}^{e} cuts. In this section, only the case of p_{T}^{e}>0.2 GeV/c is indicated. The results for p_{T}^{e}>0.4 GeV/c can be found in Appendix A.1.

Figure 4.4 shows the preliminary invariant mass spectrum [67] compared to the dielectron cocktail. The invariant mass spectrum corrected for the total pair reconstruction efficiency is calculated by:

$$\frac{1}{N_{evt}}\frac{\mathrm{d}N}{\mathrm{d}m_{\mathrm{ee}}} = \frac{1}{N_{evt}}\frac{\mathrm{d}N_{\mathrm{ee}}}{\mathrm{d}m_{\mathrm{ee}}}\frac{1}{\epsilon_{ee}^{total}} \tag{4.2}$$

where N_{evt} is number of events, $\mathrm{d}N_{\mathrm{ee}}$ is number of e^+e^- pairs and ϵ_{ee}^{total} is the pair efficiency.

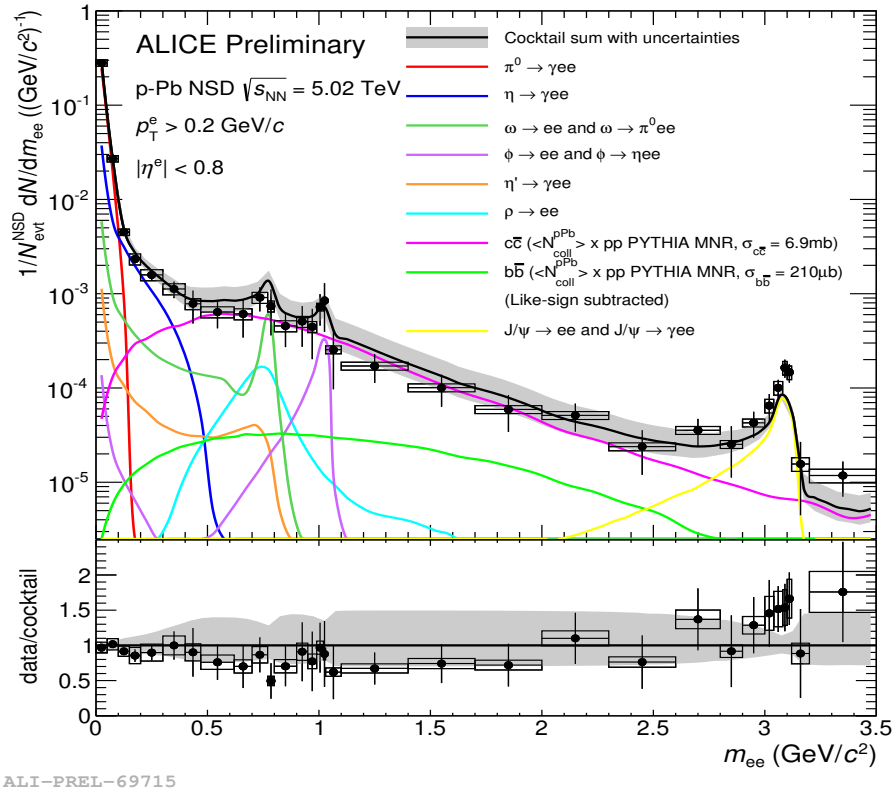

Figure 4.4.: Invariant mass spectrum from preliminary analysis compared to the dielectron cocktail in p–Pb collisions at $\sqrt{s_{\mathrm{NN}}} = 5.02$ TeV for $p_{\mathrm{T}}^e > 0.2$ GeV/c.

The data and the dielectron cocktail are in agreement within their systematic uncertainties. However, the ratio is slightly suppressed especially in the IMR where the $c\bar{c}$ contribution is dominating. Therefore, $c\bar{c}$ tuning and generation still need to be investigated in the dielectron cocktail.

In addition to invariant mass, four pair p_{T}-spectra up to 3 GeV/c in various invariant mass slices are analyzed [67]. The results of p_{T}^{ee}-spectra for m_{ee}<0.14 GeV/c^2, 0.14<m_{ee}<0.75 GeV/c^2, 0.75<m_{ee}<1.1 GeV/c^2 and 1.1<m_{ee}<3.0 GeV/c^2 are indicated in Figure 4.5 and Figure 4.6. There is a small enhancement towards higher p_{T}^{ee} in the first and second invariant mass slices (in Figure 4.5), while the data and cocktail agree well in the third and fourth slices (Figure 4.6).

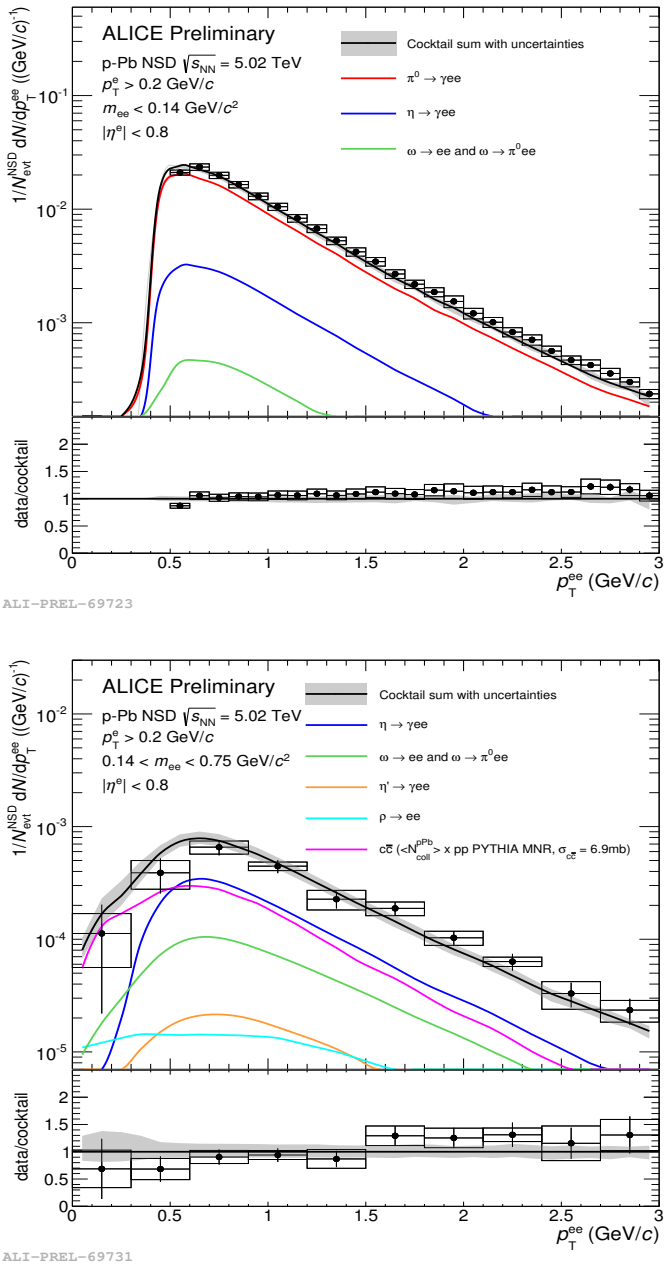

Figure 4.5.: Pair $p_{\rm T}$-spectra in the invariant mass slices of $m_{\rm ee}$<0.14 GeV/c^2 (upper panel) and 0.14<$m_{\rm ee}$<0.75 GeV/c^2 (lower panel) for $p_{\rm T}^{e}$ > 0.2 GeV/c.

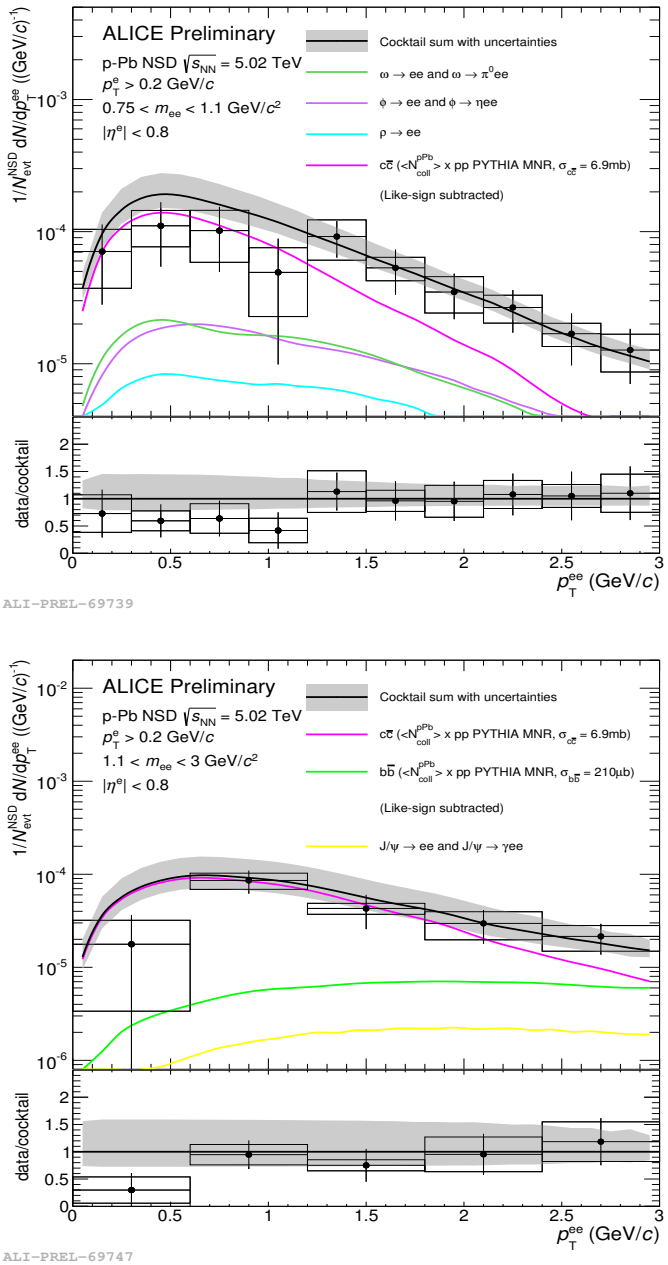

Figure 4.6.: Pair p_{T}-spectra in the invariant mass slices of $0.75<m_{\mathrm{ee}}<1.1$ GeV/c^2 (upper panel) and $1.1<m_{\mathrm{ee}}<3.0$ GeV/c^2 (lower panel) for $p_{\mathrm{T}}^{\mathrm{e}} > 0.2$ GeV/c.

4.3. Dielectron cocktail in central and semi-central Pb–Pb collisions at $\sqrt{s_{\mathrm{NN}}} = 2.76$ TeV

Since the Pb–Pb analysis is still ongoing, the data [73] analyzed up to $m_{\mathrm{ee}} = 0.5$ GeV/c^2 are not final and systematic uncertainties on the data have not been calculated yet. As in p–Pb collisions, the yield of e^+e^- pairs is calculated according to Equation 4.2.

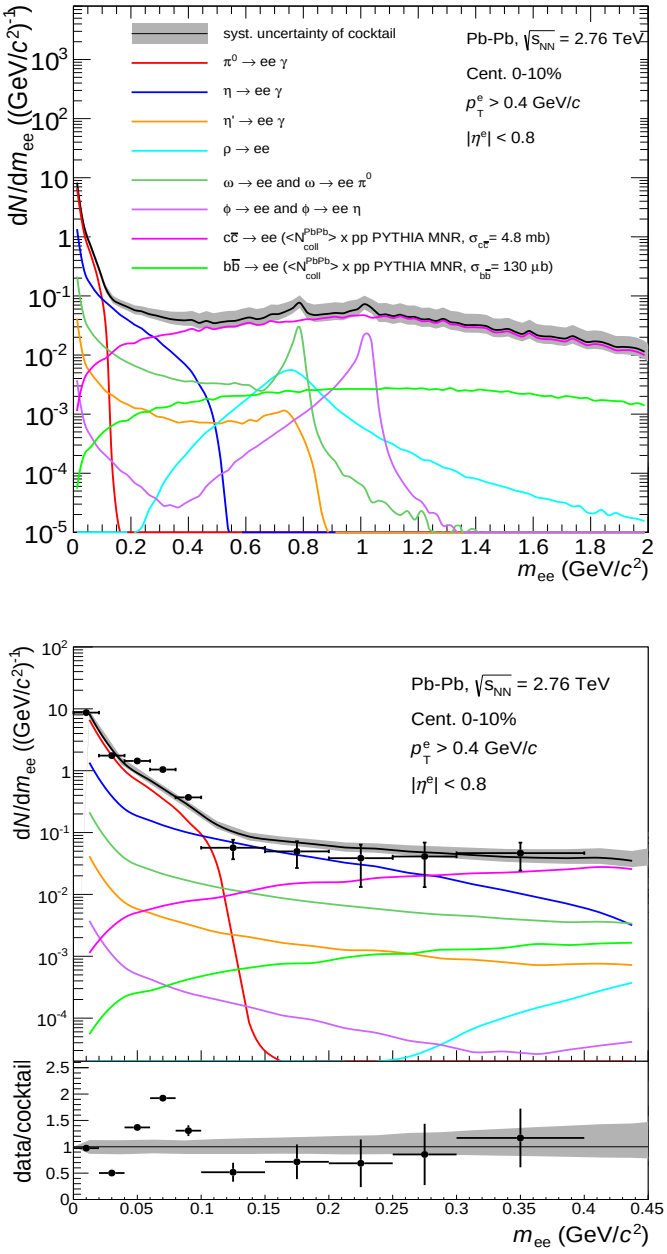

Figure 4.7.: Dielectron cocktail shown up to 2 GeV/c^2 (upper panel) and invariant mass spectrum (work in progress) compared to the dielectron cocktail (lower panel) in central (0-10%) Pb–Pb collisions at $\sqrt{s_{\mathrm{NN}}} = 2.76$ TeV.

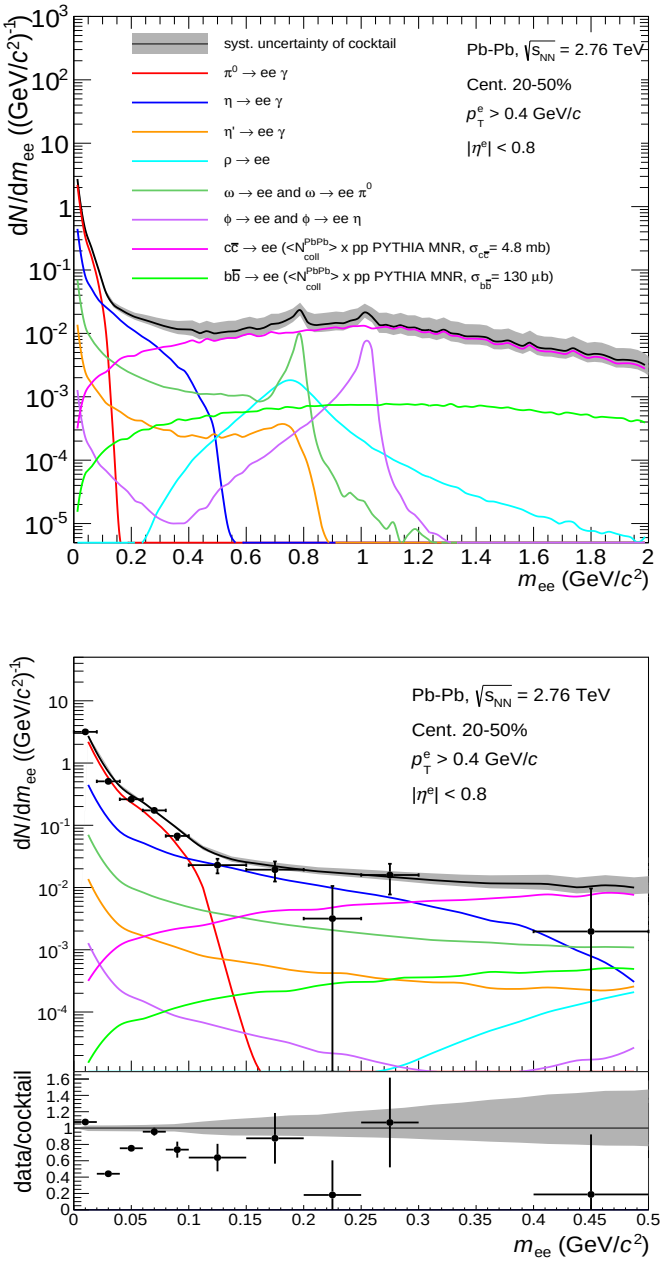

Figure 4.8.: Dielectron cocktail shown up to 2 GeV/c^2 (upper panel) and invariant mass spectrum (work in progress) compared to the dielectron cocktail (lower panel) in semi-central (20-50%) Pb–Pb collisions at $\sqrt{s_{NN}}$ = 2.76 TeV.

The results on the dielectron cocktails in central (0-10%) and semi-central (20-50%) Pb–Pb collisions are shown in Figure 4.7 and in Figure 4.8, respectively. The upper panels in Figures show the dielectron cocktails up to m_{ee} = 2 GeV/c^2 and lower panels indicate the invariant mass spectra analyzed up to m_{ee} = 0.5 GeV/c^2 compared to the corresponding dielectron cocktails.

5. Summary

This thesis presents the calculation of dielectron cocktails in minimum bias proton-proton (pp) collisions at $\sqrt{s}$ = 7 TeV, proton-lead (p–Pb) collisions at $\sqrt{s_{\rm NN}}$ = 5.02 TeV and in central (0-10%) and semi-central (20-50%) lead-lead (Pb–Pb) collisions at $\sqrt{s_{\rm NN}}$ = 2.76 TeV in the acceptance of the ALICE (A Large Ion Collider Experiment) central barrel detectors at the LHC (Large Hadron Collider). Since the calculation of the dielectron cocktails in p–Pb and Pb–Pb collisions is based on scaling of events from pp collisions, hot/cold nuclear matter effects are not considered in this dielectron cocktail study.

As the first step of the cocktail study, a new hybrid dielectron cocktail framework based on EXODUS and PYTHIA is developed, in order to correctly describe line shapes of resonances and the Dalitz decays in the low mass region (LMR). The reason behind creating a new framework is the fact that the resonance decays of ρ, ω, ϕ and the Dalitz decays of π^0, η, η', ω, ϕ are not correctly implemented by PYTHIA. In this hybrid framework, PYTHIA is kept as primary event generator, in which normalization (according to branching ratios) and decay selections are performed. EXODUS is used as decayer, in which the Dalitz decays of π^0, η, η', ω, ϕ are defined by the Kroll-Wada function while the resonance decays of ρ, ω, ϕ are defined by the Gounaris-Sakurai function. The codes for the decay kinematics from EXDOUS are used to write a new class called *AliDecayerExodus* which is adapted to PYTHIA and included into AliRoot (ALICE offline framework). Accordingly, the *AliDecayerExodus* class allows to simulate dielectron contributions of the Dalitz and resonance decays in the LMR by using the PYTHIA decay table and then by replacing the particle decay kinematics from PYTHIA by those from EXODUS.
Dielectron contributions of $c\bar{c}$ and $b\bar{b}$ which dominate the intermediate mass region (IMR) are simulated using the PYTHIA MNR (Mangano,Nison,Ridolfi) framework to produce semileptonic heavy-flavor decays in a reasonable agreement with Next to Leading Order perturbative Quantum ChromoDynamics (NLO pQCD) calculations. In the high mass region (HMR), dielectrons from J/ψ taken from full Monte Carlo (MC) simulation are generated with the EvtGen package and PHOTOS. Using PHOTOS, the effect of radiative corrections in decays are simulated. PHOTOS considers the radiative decays of J/ψ ($\rightarrow ee\gamma$) which are not taken into account by PYTHIA.
In order to generate dielectron cocktails for various collision systems, several inputs are used. In the LMR, transverse momentum spectra of π^0 and $\pi^{\pm}$ serve as main inputs which are taken from ALICE data. To produce the dielectron cocktail in pp collisions at $\sqrt{s}$ = 7 TeV, measured $p_{\rm T}$-spectra of π^0 and η from the PHOS+PCM combined method (Photon Spectrometer + Photon Conversion Method) are used. For the dielectron cocktail in p–Pb collisions at $\sqrt{s_{\rm NN}}$ = 5.02 TeV, $p_{\rm T}$-spectra of $\pi^{\pm}$ are the main inputs, which are used as an approximation of π^0 ($(\pi^+ + \pi^-)/2$). They are measured with the TPC+TOF (Time Projection Chamber and Time of Flight) up to 2.5 GeV/c and with the TPC from 2.5 up to 20 GeV/c. In Pb–Pb collisions at $\sqrt{s_{\rm NN}}$ = 2.76 TeV, both neutral and charged pion inputs are available. In central Pb–Pb collisions, the $p_{\rm T}$-spectrum of π^0 measured using the PCM serves as the main cocktail input. For the dielectron cocktail in semi-central

Pb–Pb collisions, p_{T}-spectra of $\pi^{\pm}$ from the TPC+TOF serve as the main input and are used as an approximation of π^0. p_{T}-spectra of the other light mesons (η, η', ρ, ω, ϕ) are parametrized using transverse mass scaling ($m_{\mathrm{T}} - scaling$) of pion spectra (except η in pp collisions). To obtain contributions of $c\bar{c}$, $b\bar{b}$ and J/ψ for required collision systems in the IMR and HMR, distributions of these particles are scaled by measured cross sections in ALICE of each particle and by number of binary collisions from Glauber Modeling.
Since electrons can lose a considerable part of their energy by interacting with the detector material, the effect of bremsstrahlung needs to be taken into account. The bremsstrahlung effect is implemented in full MC simulations of each collision system using a detailed description of the ALICE detector. For the purpose of the dielectron cocktail study, the distribution of momentum resolution $\Delta p/p$ vs. momentum p is extracted. Individual momentum slices are fitted in the peak region with the Landau function convoluted with the generalized Gaussian to parametrize momentum resolution. The tail of $\Delta p/p$ fitted with an exponential function gives parametrizations for the bremsstrahlung effect. Afterwards, the momenta of electrons are smeared using extracted parametrizations and invariant masses are recalculated accordingly.
Lastly, the systematic uncertainties on the dielectron cocktail are calculated. Since the uncertainty on pion cross section/yield is the major systematic error source in the LMR, errors from the pion measurement are mainly used. In order to estimate systematic errors from the pion measurement, pion data are shifted up and down by their systematic uncertainties and re-fitted. After re-fitting, the extracted parameterizations are used to reproduce dielectron cocktails for lower and upper errors. Afterwards, the systematic errors coming from the other light mesons (η, η', ρ, ω, ϕ) are determined by systematic errors on meson-to-pion ratios which are used for $m_{\mathrm{T}} - scaling$. Systematic errors coming from $c\bar{c}$, $b\bar{b}$ and J/ψ are assigned by systematic errors of their measured cross sections. Finally, the total systematic error is calculated by adding individual contributions in quadrature and by averaging upper and lower uncertainties.

As results of this thesis, the generated dielectron cocktails are compared to ALICE data. Comparison of the latest invariant mass spectrum and the dielectron cocktail in pp collisions at $\sqrt{s} = 7$ TeV shows a good agreement within their systematic uncertainties in the IMR and HMR. However, the data are still below the cocktail in the LMR especially around 0.5 GeV/c^2. The preliminary invariant mass spectrum and the dielectron cocktail in p–Pb collisions at $\sqrt{s_{\mathrm{NN}}} = 5.02$ TeV agree well. Additionally to the m_{ee} spectrum in p–Pb collisions, four pair p_{T}-spectra up to 3 GeV/c in the invariant mass slices of m_{ee}<0.14 GeV/c^2, 0.14<m_{ee}<0.75 GeV/c^2, 0.75<m_{ee}<1.1 GeV/c^2 and 1.1<m_{ee}<3.0 GeV/c^2 are compared to the dielectron cocktail. The p_{T}^{ee}-spectra in m_{ee}<0.14 GeV/c^2 and 0.14<m_{ee}< 0.75 GeV/c^2 indicate a small enhancement where the other p_{T}^{ee}-spectra show a good agreement with data. From the comparison of the dielectron cocktails to the data in central and semi-central Pb–Pb collisions at $\sqrt{s_{\mathrm{NN}}} = 2.76$ TeV, it is difficult to conclude, and the Pb–Pb data analysis is still ongoing.

6. Outlook

Dielectron cocktails generated within this work are generally in good agreement with data taken in pp, p–Pb and Pb–Pb collisions. Furthermore, the PHYTIA MNR framework for $c\bar{c}$ and $b\bar{b}$ works properly. However, $c\bar{c}$ and $b\bar{b}$ contributions still need to be investigated to consider their complicated kinematics precisely. Also triggered data for higher p_{T} are taken in ALICE for pp and p–Pb collisions. Triggered data are interesting to study high mass resonances like J/ψ and also Drell-Yan contribution. One of the future plans for the dielectron cocktail study is the implementation of the Drell-Yan kinematics. Besides the kinematics of particles, the parametrization library for cocktail input (*AliGenEMlib*) must be kept up-to-date, so new parameters (once they exist) will be added into the *AliGenEMlib* class.

A. Appendix

A.1. Dielectron cocktail results in p–Pb collisions at $\sqrt{s_{\mathrm{NN}}}$ = 5.02 TeV for p_{T}^{e}>0.4 GeV/c

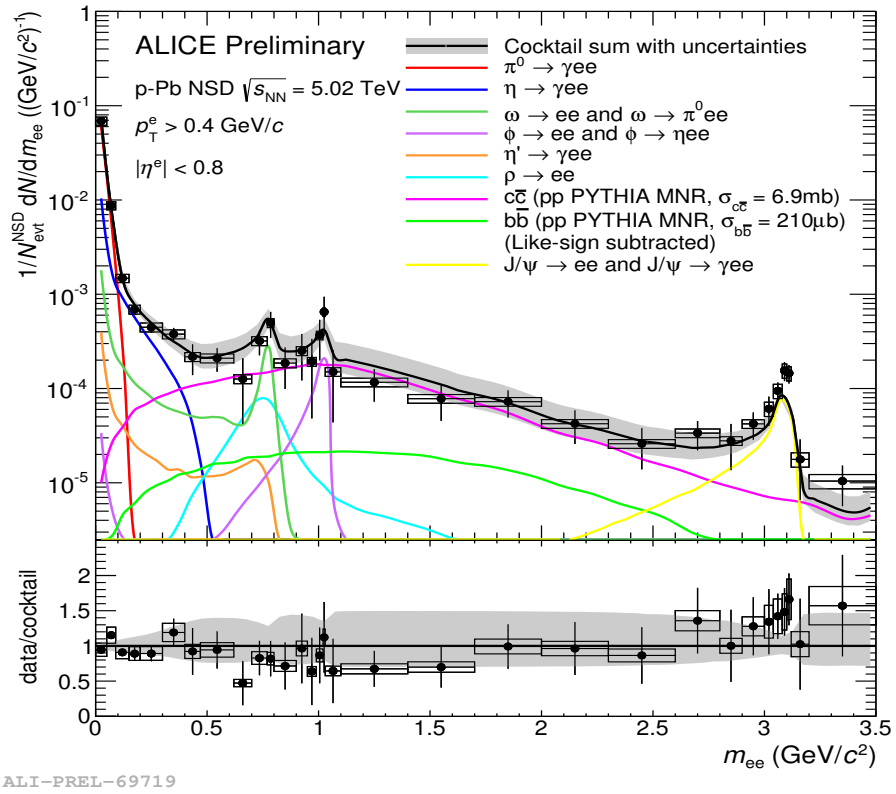

Figure A.1.: Invariant mass spectrum from preliminary analysis compared to the dielectron cocktail in p–Pb collisions at $\sqrt{s_{\mathrm{NN}}}$ = 5.02 TeV for p_{T}^{e} > 0.4 GeV/c.

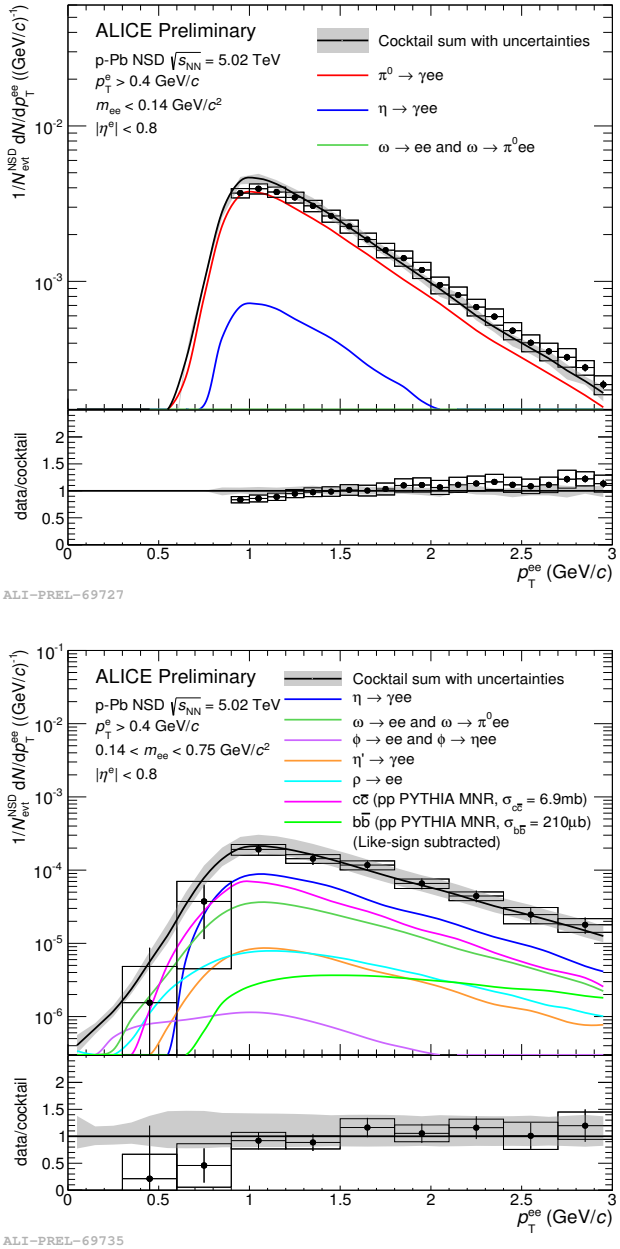

Figure A.2.: Pair p_{T} spectra in the invariant mass slices of m_{ee}<0.14 GeV/c^2 (upper panel) and 0.14<m_{ee}<0.75 GeV/c^2 (lower panel) for $p_{\mathrm{T}}^e > 0.4$ GeV/c.

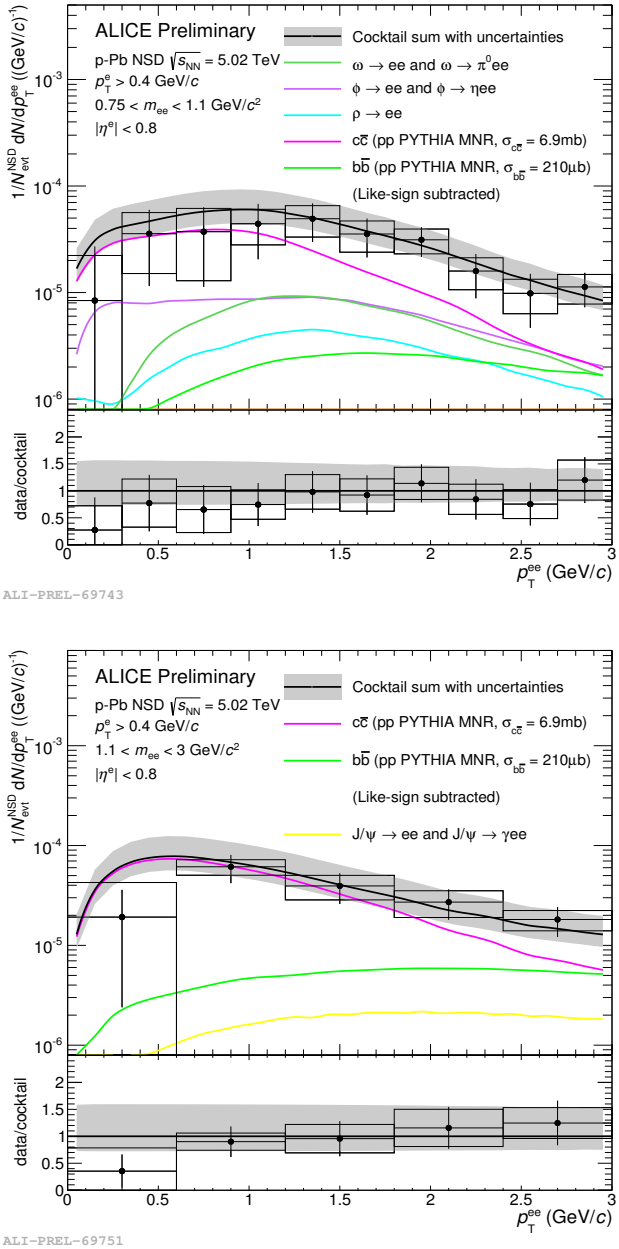

Figure A.3.: Pair p_{T} spectra in the invariant mass slices of 0.75<m_{ee}<1.1 GeV/c^2 (upper panel) and 1.1<m_{ee}<3.0 GeV/c^2 (lower panel) for p_{T}^{e} > 0.4 GeV/c.

List of Figures

List of Tables

Bibliography

[1] C. Y. Wong, *Introduction to High-Energy Heavy-Ion Collisions* (World Scientific, 1994).

[2] R. Stock, *Relativistic Nucleus-Nucleus Collisions and the QCD Matter Phase Diagram*, arXiv:nucl-ex/0807.1610v1 (2008).

[3] B. Müller, *Investigation of Hot QCD Matter: Theoretical Aspects*, arXiv:nucl-th/1309.7616v2 (2013).

[4] F. Karsch, *Lattice QCD at High Temperature and Density*, arXiv:hep-lat/0106019v2 (2001).

[5] R. Rapp and J. Wambach, *Chiral Symmetry Restoration and Dileptons in Relativistic Heavy-Ion Collisions*, arXiv:hep-ph/9909229v1 (1999).

[6] CBM Collaboration, *The Compressed Baryonic Matter Experiment*, http://www-alt.gsi.de/documents/DOC-2007-Apr-21-1.pdf (2008).

[7] Physics and Universe, *Standard Model of The Big Bang Theory*, http://physicsanduniverse.com/standard-model-of-the-big-bang-theory/ .

[8] B. Povh, K. Rith, C. Scholz and F. Zetsche, *Particles and Nuclei* (Springer, 2008).

[9] A. Lamont, *Neutral Strange Particle Production in Ultra-Relativistic Heavy Ion Collissions at* $\sqrt{s_{NN}} = 130GeV$, PhD thesis, The University of Birmingham, 2002.

[10] A. Seiden, *Particle Physics - A Comprehensive Introduction* (Addison Wesley, 2005).

[11] Particle Data Group, Chin. Phys. C **38**, 010009 (2014).

[12] L. P. Csernai, *Introduction to Relativistic Heavy Ion Collisions* (John Wiley and Sons Ltd., 1994).

[13] V. Koch, *Introduction to Chiral Symmetry*, arXiv:nucl-th/9512029 (1995).

[14] M. Ablikim et al. (BESIII Collaboration), *Measurements of the mass and width of the* η_c *using* $\Psi(3686) \to \gamma\eta_c$, Phys. Rev. Lett. **108**, 222002 (2012).

[15] J. J. Aubert et. al., *Experimental Observation of Heavy Particle J*, Phys. Rev. Lett. **33**, 1404 (1974).

[16] J.-E. Augustin et. al., *Discovery of a Narrow Resonance in* e^+e^- *Annihilation*, Phys. Rev. Lett. **33**, 1406 (1974).

[17] B. Aubert et al. (BABAR Collaboration), *Observation of the Bottomonium Ground State in the Decay* $\Upsilon(3S) \to \gamma\eta_b$, Phys. Rev. Lett. **101**, 071801 (2008).

[18] S. W. Herb et. al., *Observation of a Dimuon Resonance at 9.5 GeV in 400-GeV Proton-Nucleus Collisions*, Phys. Rev. Lett. **39**, 252 (1977).

[19] W. R. Innes et. al., *Observation of Structure in the* Υ *Region*, Phys. Rev. Lett. **39**, 1240 (1977).

[20] D. H. Perkins, *Introduction to High Energy Physics* (Cambridge University Press, 2000).

[21] A. Drees, *Dileptons And Photons At RHIC Energies*, arXiv:nucl-ex/0909.4976 - Nucl. Phys. A **830**, 435c (2009).

[22] T. Matsui and H. Satz, J/ψ *Suppression by Quark-Gluon Plasma Formation*, Phys. Lett. **B 178**, 416 (1986).

[23] G. E. Brown and M. Rho, *Chiral restoration in hot and/or dense matter*, Phys. Rep. **269**, 333 (1996).

[24] T. Galatyuk, *Di-electron spectroscopy in HADES and CBM: from p + p and n + p collisions at GSI to Au + Au collisions at FAIR*, PhD thesis, Goethe Universität Frankfurt, 2009.

[25] CERES Collaboration, *Modification of the* ρ *meson detected by low-mass electron-positron pairs in central Pb-Au collisions at 158A GeV/c*, arXiv:nucl-ex/0611022v3 - Phys. Lett. B **666**, 425 (2008).

[26] ALICE Collaboration, *The ALICE Experiment at the CERN LHC*, JINST **3**, S08002 (2008).

[27] ALICE Collaboration, *ALICE: Physics Performance Report, Volume 1*, Journal of Physics G: Nuclear and Particle Physics **30**, 1517 (2004).

[28] ALICE Collaboration, *ALICE: Physics Performance Report, Volume 2*, Journal of Physics G: Nuclear and Particle Physics **32**, 1295 (2006).

[29] ALICE Collaboration, *Technical Design Report of the Inner Tracking System*, CERN/LHCC 99-12 (1999).

[30] ALICE Collaboration, *Technical Design Report of the Time Projection Chamber*, CERN/LHCC 2000-001 (2000).

[31] ALICE Collaboration, *Upgrade of the ALICE Experiment Letter Of Intent*, CERN-LHCC-2012-012 (2012).

[32] ALICE Collaboration, *Technical Design Report of the Transition Radiation Detector*, CERN /LHCC 2001-021 (2001).

[33] ALICE Collaboration, *The ALICE Offline Bible*, http://aliweb.cern.ch/secure/Offline/sites/aliweb.cern.ch.Offline/files/uploads/OfflineBible.pdf .

[34] *ROOT Data Analysis Framework*, http://root.cern.ch/ .

[35] T. Sjöstrand, S. Mrenna and P. Skands, *PYTHIA 6.4 Physics and Manual*, arXiv:hep-ph/0603175 (2006).

[36] PHENIX Collaboration, *Detailed measurement of the e^+e^- pair continuum in p+p and Au+Au collisions at $\sqrt{s_{NN}}$ = 200 GeV and implications for direct photon production*, arXiv:nucl-ex/0912.0244 - Phys. Rev. C **81**, 034911 (2010).

[37] PHENIX Collaboration, http://www.phenix.bnl.gov .

[38] N. M. Kroll and W. Wada, *Internal Pair Production Associated with the Emission of High-Energy Gamma Rays*, Phys. Rev. **98**, 5 (1955).

[39] L. Landsberg, *Electromagnetic Decays of Light Mesons*, Phys. Rev. Lett. **128**, 6 (1985).

[40] G.J.Gounaris and J.J.Sakurai, *Finite-Width Corrections to the Vector-Meson-Dominance Prediction for $\rho \to e^+e^-$*, Phys. Rev. Lett. **21**, 244 (1968).

[41] ALICE Collaboration, *B. Abelev et al. "Neutral pion and η meson production in proton-proton collisions at $\sqrt{s}$ = 0.9 TeV and 7 TeV"*, Physics Letters B **717**, 162 (2012).

[42] Y. Kharlov for ALICE Collaboration, *Neutral meson production in pp and Pb-Pb collisions at LHC*, arXiv:nucl-ex/1208.4712v1 (2012).

[43] C. Tsallis, *Possible Generalization of Boltzmann-Gibbs Statistics*, J.Statist.Phys. **52**, 479 (1988).

[44] ALICE Collaboration, *J. Wagner "Measurement of electrons from semi-leptonic heavy-flavor hadron decays in p-Pb collisions at $\sqrt{s_{NN}}$ = 5.02 TeV"*, (2014).

[45] R. Hagedorn, *Multiplicities, p_T distributions and the expected hadron $\to$ quark-gluon phase transition*, La Rivista del Nuovo Cimento **6**, 10 (1983).

[46] Private communication with Martin Wilde.

[47] ALICE Collaboration, *Centrality Dependence of π, K, p Production in Pb–Pb Collisions at $\sqrt{s_{NN}}$ = 2.76 TeV*, arXiv:hep-ex/1303.0737 (2014).

[48] S. S. Adler et al. (PHENIX), *High transverse momentum η meson production in p+p,d+Au, and Au+Au collisions at $\sqrt{s_{NN}}$ = 200 GeV*, Phys. Rev. **C75**, 024909 (2007).

[49] S. S. Adler et al. (PHENIX), *Production of ω mesons at large transverse momenta in p+p and d+Au collisions at $\sqrt{s_{NN}}$ = 200 GeV*, Phys. Rev. **C75**, 051902 (2007).

[50] V. Ryabov et al., Nucl. Phys. **A774**, 735 (2006).

[51] M. Mangano, P. Nason and G. Ridolfi, *Heavy-quark correlations in hadron collisions at next-to-leading order*, Nucl. Phys. **B373**, 295 (1992).

[52] J. Pumplin *et al.*, *New Generation of Parton Distributions with Uncertainties from Global QCD Analysis*, arxiv:hep-ph/0201195v3 (2002).

[53] ALICE Collaboration, *Measurement of charm production at central rapidity in proton–proton collisions at $\sqrt{s}$ = 2.76 TeV*, arXiv:hep-ex/1205.4007v2 (2012).

[54] ALICE Collaboration, *Beauty production in pp collisions at $\sqrt{s}$ = 2.76 TeV measured via semi-electronic decays*, arXiv:nucl-ex/1405.4144v1 (2014).

[55] ALICE Collaboration, *Measurement of electrons from beauty hadron decays in pp collisions at $\sqrt{s}$ = 7 TeV*, arXiv:hep-ex/1208.1902v3 (2013).

[56] M. Cacciari, M. Greco and P. Nason, *The p_T Spectrum in Heavy-Flavour Hadroproduction*, arXiv:hep-ph/9803400v1 (1998).

[57] M. Cacciari, S. Frixione and P. Nason, *The p_T Spectrum in Heavy-Flavour Photoproduction*, arXiv:hep-ph/0102134v1 (2001).

[58] M. L. Miller, K. Reygers, S. J. Sanders and P. Steinberg, *Glauber Modeling in High Energy Nuclear Collisions*, arXiv:nucl-ex/0701025v1 (2007).

[59] B. Alver, M. Baker, C. Loizides and P. Steinberg, *The PHOBOS Glauber Monte Carlo*, arXiv:nucl-ex/0805.4411 (2008).

[60] A. Toia on behalf of the ALICE Collaboration, *ALICE Measurement in p–Pb Collisions: Charged Particle Multiplicity, Centrality Determination and implications for Binary Scaling*, arXiv:nucl-ex/1403.5143 (2013).

[61] ALICE Collaboration, *Centrality determination of Pb–Pb collisions at $\sqrt{s_{NN}}$ = 2.76 TeV with ALICE*, arXiv:nucl-ex/1301.4361v3 (2014).

[62] D. J. Lange, *The EvtGen particle decay simulation package*, Nucl. Instrum. Meth. **A462** (2001).

[63] E. Barberio, B. van Eijk and Z. Was, *Photos as a universal Monte Carlo for QED radiative corrections in decays*, Comput. Phys. Commun. **66** (1991).

[64] E. Barberio and Z.Was, *PHOTOS: A Universal Monte Carlo for QED radiative corrections. Version 2.0*, Comput. Phys. Commun. **79** (1994).

[65] ALICE Collaboration, *Erratum to Rapidity and transverse momentum dependence of inclusive J/ψ production in pp collisions at $\sqrt{s}$ = 7 TeV*, Physics Letters B **718** (2012).

[66] M. K. Köhler, *Low-mass dielectron measurement in pp and Pb–Pb collisions in ALICE*, arXiv:hep-ex/1302.2049v1 (2013).

[67] T. Bröker, https://indico.cern.ch/event/219436/session/2/contribution/155 .

[68] ALICE Collaboration, *Rapidity and transverse momentum dependence of inclusive J/ψ production in pp collisions at $\sqrt{s}$ = 7 TeV*, arXiv:hep-ex/1105.0380 (2012).

[69] M. Winn on behalf of the ALICE Collaboration, *Inclusive J/ψ and ψ(2S) production in p–Pb collisions at $\sqrt{s_{NN}}$ = 5.02 TeV with ALICE at the LHC*, arXiv:hep-ex/1404.1615 (2013).

[70] R. Bailhache, *Calibration of the ALICE Transition Radiation Detector and a study of Z^0 and heavy quark production in pp collisions at the LHC*, PhD thesis, TU Darmstadt, 2009.

[71] ALICE Collaboration, *Measurement of inelastic, single- and double-diffraction cross sections in proton-proton collisions at the LHC with ALICE*, arXiv:hep-ex/1208.4968 - Eur. Phys. J. C **73**, 2456 (2013).

[72] Private communication with Markus K. Köhler.

[73] Private communication with Alberto Caliva.

Acknowledgements

It would not have been possible to realise this work without the help and support of many people whom I ought to thank.
First of all, I would like to express my gratitude to Prof. Dr. Harald Appelshäuser who gave me the opportunity to join the ALICE working group at the IKF and to provide me this thesis in an interesting field of physics. Moreover, I am grateful to him for the endless support and encouragement to this study. I have learnt much more from his enthusiasm about science. I also thank to my second supervisor Prof. Dr. Christoph Blume for reading and evaluating this thesis.
I ought to thank Dr. Ralf Averbeck, who is a pioneer of the dielectron cocktail study, for helpful discussions and advices. Many thanks to Dr. Christoph Baumann for his support on working with cocktail inputs and on computing.
I would like to extend my thanks to all people of the Low Mass Dielectron Group of the ALICE Physics Working Group for Dileptons and Quarkonia (PWDQ). In particular, I would like to give my special thanks to Taku Gunji and Markus Köhler for fruitful discussions and endless support on the simulation of semileptonic heavy-flavor decays and the calculation of systematic uncertainties. Additionally, I thank to Markus for providing the invariant mass spectrum in pp collisions. I also thank to Giuseppe Bruno and Fiorella Fionda for helping and giving me advices on simulating J/ψ, to Patrick Reichelt for his support and helpful discussions, to Dr. Hongyan Yang and to Alberto Caliva for providing the invariant mass spectra in Pb–Pb collisions, to Theo Bröker for providing the invariant mass and pair p_{T} spectra in p–Pb collisions.
I would like to thank Dr. Raphaelle Bailhache for helping during the implementation of the bremsstrahlung effect and momentum resolution into dielectron cocktail, and Theodor Rascanu for the cooperation on working with the parametrization library for cocktail inputs.
I also thank to Prof. Dr. Henner Büsching, Dr. Benjamin Dönigus, Simone Schuchmann, Julian Book, Stefan Heckel, Philipp Lüttig, Esther Bartsch, Carsten Klein and Fabian Pliquett for their companionship in the field and also for their friendship. I also want to express my gratitude to Werner Amend and Ulrich Köpf for the help whenever I needed and for the positive atmosphere at the institute.
I ought to thank Dr. Anar Rustamov for fruitful discussions on the dielectron cocktail study, and Mesut Arslandok for his support on computing and also on the implementation of the bremsstrahlung effect and momentum resolution. Additionally, I would like to thank them for the memorable friendship. I also thank to Dr. Günnur Görücü Güler and Zehra Deveci for the good time in Frankfurt and especially for their valuable friendship.
I would like to give my very special thanks to my parents. Without their endless patient and support during all this time I could not manage to fulfill this thesis.
Finally, I express my thankfulness to my husband, my friend and my colleague Mahmut Özdemir for supporting and enduring me not only in the field but also during all this time.

Eidesstattliche Erklärung

Hiermit erkläre ich, dass ich diese Arbeit selbstständig und ohne Benutzung anderer als der angegebenen Quellen und Hilfsmittel verfasst habe. Alle Stellen der Arbeit, die wörtlich oder sinngemäß aus Veröffentlichungen oder aus anderen fremden Texten entnommen wurden, sind von mir als solche kenntlich gemacht worden. Ferner erkläre ich, dass die Arbeit nicht - auch nicht auszugsweise - für eine andere Prüfung verwendet wurde.

Frankfurt am Main, den 11.11.2014

İrem Erdemir Özdemir